Acta Pharmaceutica Sinica B 2026;16(6):3802−3827

Chinese Pharmaceutical Association
Institute of Materia Medica, Chinese Academy of Medical Sciences

Acta Pharmaceutica Sinica B

www.elsevier.com/locate/apsb
www.sciencedirect.com

ORIGINAL ARTICLE

Discovery of sulfonyl benzoic acid derivatives with joint TGR5-agonist and FXR-antagonist activity for myocardial ischemia/reperfusion injury protection

Xinyi Zhao[a,†], Tianqi Chang[b,†], Xiang Wu[d,†], Tongyu Huo[a,†], Jing Peng[a], Yameng Liu[a], Dongfang Li[d], Chao Wang[a], Fan Yang[d], Jiaxing Wang[b,*], Xiaodong Dou[a,*], Jinpeng Sun[d,*], Ming Xu[b,c,*], Ning Jiao[a,e,*]

[a]*State Key Laboratory of Natural and Biomimetic Drugs, Beijing Key Laboratory of AI-Driven Drug Discovery and Development, New Cornerstone Science Laboratory, Chemical Biology Center, School of Pharmaceutical Sciences, Peking University, Beijing 100191, China*
[b]*Department of Cardiology and Institute of Vascular Medicine, Peking University Third Hospital, State Key Laboratory of Vascular Homeostasis and Remodeling, NHC Key Laboratory of Cardiovascular Molecular Biology and Regulatory Peptides, Beijing Key Laboratory of Cardiovascular Receptors Research, Peking University, Beijing 100191, China*
[c]*Research Unit of Medical Science Research Management/Basic and Clinical Research of Metabolic Cardiovascular Diseases, Chinese Academy of Medical Sciences, Beijing 100191, China*
[d]*Key Laboratory Experimental Teratology of the Ministry of Education and Department of Biochemistry and Molecular Biology, School of Basic Medical Sciences, Cheeloo College of Medicine, Shandong University, Jinan 250012, China*
[e]*Laboratory for Synthetic Chemistry and Chemical Biology Limited, Health@InnoHK, Innovation and Technology Commission, Hong Kong SAR, China*

Received 1 June 2025; received in revised form 20 October 2025; accepted 5 November 2025

*Corresponding authors.
E-mail addresses: wangjiaxing3969@163.com (Jiaxing Wang), xddou@pku.edu.cn (Xiaodong Dou), sunjinpengsdu@126.com (Jinpeng Sun), xuminghi@bjmu.edu.cn (Ming Xu), jiaoning@pku.edu.cn (Ning Jiao).
[†]These authors made equal contributions to this work.
Peer review under the responsibility of Chinese Pharmaceutical Association and Institute of Materia Medica, Chinese Academy of Medical Sciences.

https://doi.org/10.1016/j.apsb.2026.03.038

KEY WORDS

TGR5 agoninst;
FXR antagonist;
Sulfonyl benzoic acid derivative;
Structure−activity relationship;
Myocardial ischemia/reperfusion injury;
Left ventricular ejection fraction;
Infarct size;
Cardioprotective mechanism

Abstract TGR5 and FXR are key regulators of metabolic homeostasis and cardiovascular health. Since the cardioprotective capacity of TGR5 activation and FXR inhibition has been recognized, dual modulation of these targets offers a promising therapeutic strategy for myocardial ischemia/reperfusion injury. Herein, sulfonyl benzoic acid derivatives were identified as effective bidirectional modulators, with compound **E6** emerging as a potent lead compound. **E6** demonstrated robust dual-target activity, significantly preserving cardiomyocyte viability and attenuated reactive oxygen specie overproduction in hypoxia/reoxygenation models. Moreover, oral administration of **E6** markedly reduced infarct size and improved cardiac contractile function after ischemia/reperfusion *in vivo*, without inducing gallbladder-related side effects. Notably, **E6** demonstrated superior efficacy in restoring systolic function compared to monoregulators. Transcriptomic analysis and subsequent validation studies suggested that its therapeutic effects are mediated through favorable modulation of inflammatory response, attenuation of apoptosis, and enhanced cardiomyocytes survival. Our findings underscore the therapeutic advantages of dual TGR5/FXR targeting and establish **E6** as a promising bifunctional lead compound for the treatment of myocardial ischemia/reperfusion injury.

1. Introduction

Ischemic heart disease (IHD), also known as coronary artery disease, is characterized by reduced blood flow to the heart muscle due to narrowing or blockage of the coronary arteries. This condition leads to an imbalance between myocardial oxygen supply and demand, resulting in symptoms such as angina and, in severe cases, myocardial infarction. IHD remains a leading cause of mortality worldwide[1], with myocardial infarction (MI) representing its most severe manifestation[2]. Although percutaneous coronary intervention (PCI) and other reperfusion therapies have significantly reduced MI-associated mortality, the 1-year cardiovascular death rate still exceeds 11%[3]. Paradoxically, ischemia/reperfusion (I/R) injury occurs during reperfusion following ischemia, and sustained myocardial ischemia/reperfusion injury (MIRI) enlarges infarct size and exacerbates cardiac dysfunction[4]. Although ischemic conditioning and intracoronary oxygen infusion have improved clinical outcomes in MI patients, there remains a critical unmet need for a convenient pharmacological approach to cardioprotection.

The pathological progression following MI unfolds in a series of stages, encompassing early acute injury, inflammatory response, tissue proliferation and repair, and adverse remodeling[5]. Ischemia imposes energetic and hypoxic stress on cardiomyocytes, triggering intracellular acidosis, ATP depletion, and protease activation that collectively initiate cell death. Although rapid reperfusion is essential for survival and functional recovery, it simultaneously induces oxidative stress, dysregulated ion shifts, and acute inflammation, processes which culminate in lethal cardiomyocyte injury[6], vascular dysfunction[7], and myocardial edema[8]. Thus, despite its clinical benefits, the net effect of ischemia−reperfusion includes acute transmural injury and accelerated maladaptive remodeling[9], underscoring the urgent need for targeted interventions against these injury processes[10]. Given the multifactorial nature and the coexistence of diverse cell death modalities in MIRI[11], mono-therapeutic approaches that target a single mechanism often demonstrate limited clinical efficacy[12]. This disappointing translational gap between preclinical promise and clinical performance may partially attribute to metabolic heterogeneity among patient populations[13]—an often-overlooked factor during early-stage drug discovery. Moreover, pre-existing metabolic risk factors are known to worsen post-MI outcomes[14]. Therefore, there is an urgent need to discover novel therapeutic strategies that address both cardioprotection and metabolic dysregulation[15]. In complex diseases such as cancer and central nervous system (CNS) disorders, modulating multiple pathways has shown potential benefits[16]. Polypharmacological strategies not only enhance therapeutic efficacy and patient compliance but also reduce the risk of drug−drug interactions, making them a promising direction for the treatment of MIRI[12].

Bile acids (BAs) and their receptors are well-established regulators of metabolic homeostasis[17], with growing clinical evidence implicating BA dysregulation in the pathogenesis and progression of cardiovascular disease[18-20]. In addition to our previous studies demonstrating the cardioprotective effects of the membrane-bound BA receptor TGR5 (also known as G protein-coupled bile acid receptor 1, GPBAR1) in MI and other cardiovascular conditions[21-23], other research has highlighted its therapeutic potential in MIRI[24,25]. Another classic bile acid receptor, the Farnesoid X Receptor (FXR), plays an important role in the cardiovascular system by regulating key processes, such as vascular cell growth[26], mesenchymal stromal cell apoptosis[27], endothelial dysfunction[28,29] and lipid metabolism[30,31]. Pharmacological or genetic inhibition of FXR in murine models of MI[32] and MIRI[33] promotes cardiac recovery by reducing cardiomyocyte apoptosis, promoting angiogenesis and attenuating myocardial fibrosis. Given the therapeutic benefits of TGR5 activation and FXR inhibition, we propose that a dual-target strategy combining TGR5 agonism with FXR antagonism may provide both cardioprotection and metabolic regulation in the treatment of MIRI.

Despite the discovery of various TGR5 agonists[34,35] (INT777 (**1**), SB-756050 (**2**)), FXR antagonists[36-38] (Guggulsterone (**3**)) and dual agonists[39] (INT-767 (**4**)), reports of bidirectional modulators[40-46] capable of simultaneously activating TGR5 and inhibiting FXR remain scarce (Fig. 1). Several natural and steroid-derived bifunctional molecules, including curcumin[44], HDCA (**6**)[46] and Ft1 (**7**)[40], have been studied primarily for anti-obesity effects through regulation of glucose and lipid metabolism. However, reports on non-steroid bifunctional molecules (*e.g.*, compound **79a** (**5**)[41]) remain limited. Furthermore, the potential

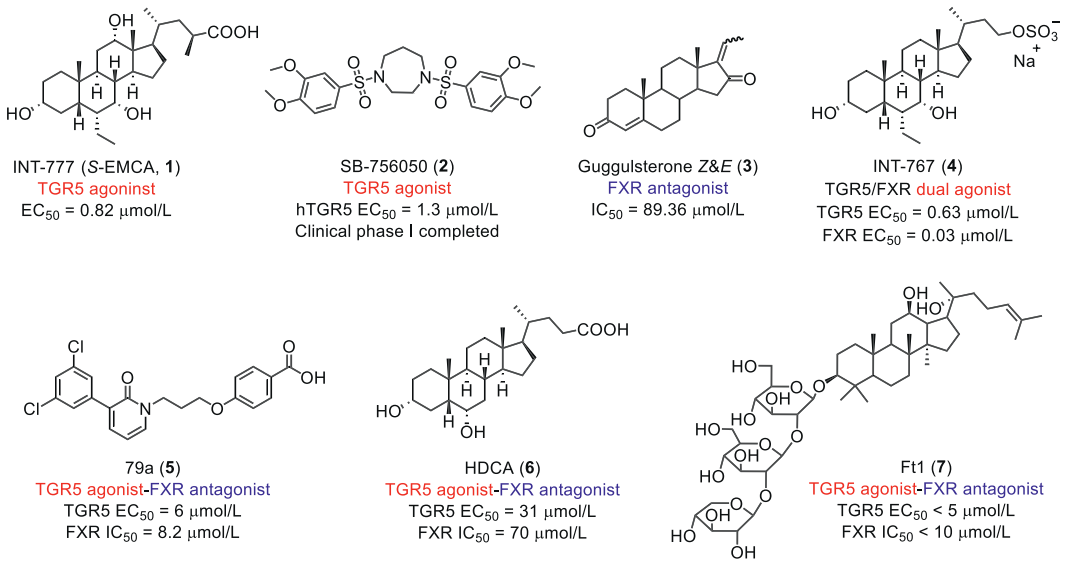

Figure 1 Representative structures of TGR5/FXR modulators. The figure shows TGR5 agonists (**1** and **2**), an FXR antagonist (**3**), a dual agonist (**4**), and TGR5 agonists but FXR antagonists (**5**, **6**, and **7**), along with their activity profiles and proposed therapeutic indications.

cardiovascular benefits mediated by dual-target modulation remain underexplored.

In this study, virtual screening combined with iterative rational design was employed to identify novel bifunctional modulators targeting both TGR5 and FXR. Among them, compound **E6** exhibited strong therapeutic potential against MIRI by reducing hypoxia/reoxygenation (H/R)-induced cardiomyocyte death and reactive oxygen species (ROS) overproduction. *In vivo* studies further confirmed its cardioprotective effect, demonstrating a favorable safety profile, reduced infarct size, decreased serum myocardial enzyme levels, and significantly improved cardiac systolic function. Further transcriptomic analyses indicate that **E6** provides advantages over mono-targeting strategies by simultaneously enhancing metabolic regulation, suppressing apoptosis, and fine-tuning inflammatory responses. These findings highlight a novel pharmacological strategy for MIRI treatment, and position **E6** as a promising lead compound for bidirectional modulation of TGR5 and FXR.

2. Results

2.1. Hit identification via TGR5-based virtual screening

Leveraging the activated TGR5 structure, our discovery of bidirectional modulators was conducted in two steps: structure-based screening for TGR5 agonists, followed by optimization to enhance FXR antagonistic activity. Given the relatively stationary nature of the orthosteric pocket in TGR5, we initiated hit identification through molecular docking studies targeting this site. At the outset, two ligand-bound TGR5 cryo-EM structures are available[47]: P395 (PDB ID: 7CFM) and INT-777 (PDB ID: 7CFN). To determine the most suitable model for virtual screening, both ligands were re-prepared and redocked into their respective binding sites using Schrödinger Glide. The redocking performance was evaluated based on root-mean-square deviation (RMSD) of the ligand pose relative to the experimental structure, and docking scores (Supporting Information Fig. S1). The redocking of P395 yielded an RMSD of 2.16 Å and a docking score of −7.27 kcal/mol, successfully reproducing the original binding conformation, including a key hydrogen bond with Tyr240—a residue recognized as a "toggle switch" critical for TGR5 activation. In contrast, the redocking of INT-777 resulted in a significantly higher RMSD of 6.71 Å and a docking score of −6.72 kcal/mol, with notable deviations in the orientation of the C24-carboxyl group and a 3.24 Å displacement at the 3-OH substituent. Due to its better reproducibility in both binding pose and predicted affinity, the TGR5 structure derived from the P395 complex (PDB ID: 7CFM) was selected as the receptor model for subsequent virtual screening.

As depicted in the hierarchical virtual screening workflow (Fig. 2A), over 220,700 molecules from both the Specs library and our in-house collection were docked into the TGR5 binding site. A multi-step filtering process was implemented to prioritize candidates for experimental validation. First, compounds with a docking score < -7.50 kcal/mol were retained to ensure sufficient predicted binding affinity. Second, molecules were required to form key interactions with residues known to be critical for TGR5 activation[47-50], including aromatic stacking with Trp75 or Phe161, as well as a hydrogen bond with Glu169 or Tyr240. Third, a similarity-based exclusion criterion was applied to maximize structural diversity among the selected hits. Following visual inspection of docking poses, 29 structurally diverse compounds were advanced for biological evaluation in a TGR5 activation assay (Supporting Information Fig. S2).

The hTGR5 agonistic activity of the 29 selected molecules was evaluated using cAMP GloSensor assay (Supporting Information Table S1). Among them, three demonstrated clear agonistic activity, with **T12** and **T26** identified as TGR5 partial agonists in the micromolar range based on dose-response curves, as measured by Emax relative to the reference agonist INT-777. The FXR activity of **T26** was further evaluated using a time-resolved fluorescence resonance energy transfer (TR-FRET) assay to investigate its effect on FXR-coactivator recruitment. The results showed that **T26** alone did not activate FXR (Supporting Information Fig. S3B), but it dose-dependently antagonized CDCA-induced FXR activation with an IC_{50} value more than 100 μmol/L (Fig. S3C). While this

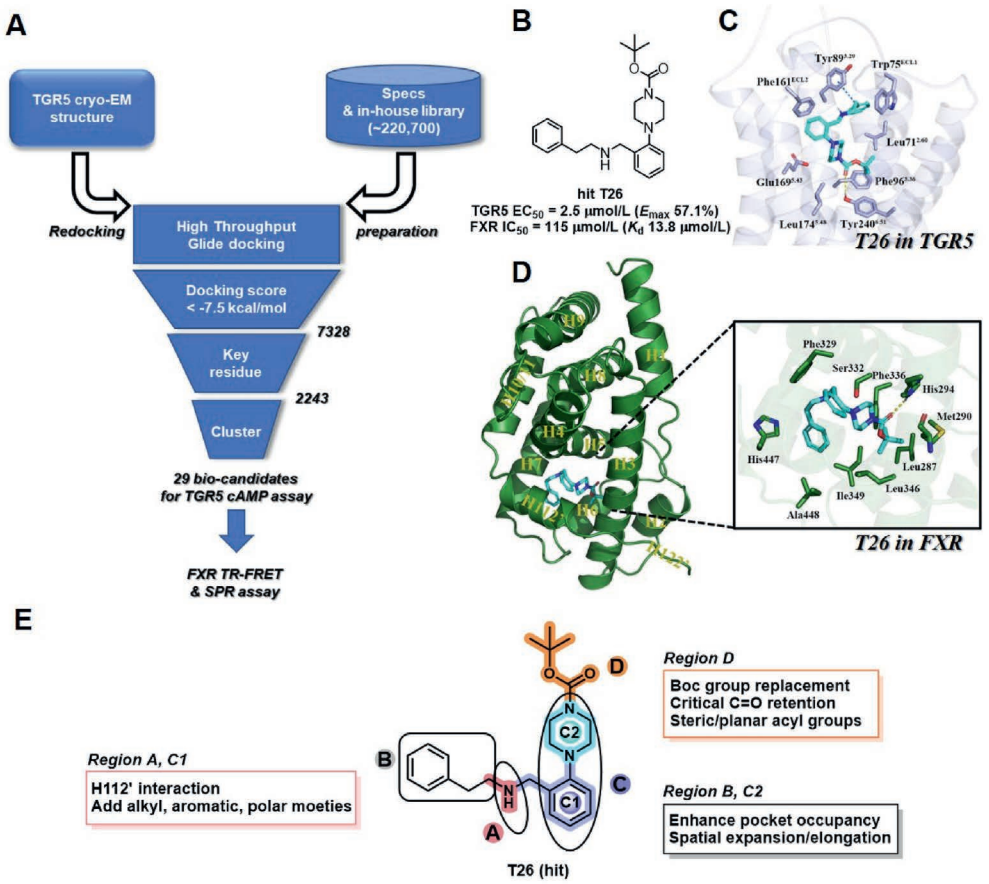

Figure 2 Hit identification. (A) Workflow of virtual and biological screening. (B) Structure and dual-target activities of hit compound **T26**. (C) Predicted binding mode of **T26** (cyan) in the TGR5 (purple) orthosteric pocket (PDB: 7CFM). (D) Predicted binding mode of **T26** (cyan) in the FXR (green) ligand-binding pocket (PDB: 4OIV). Yellow dashed lines indicate hydrogen bonds, and blue dashed lines indicate $\pi-\pi$ stacking interactions. (E) Modification strategies of hit compound **T26**.

antagonistic effect was relatively weak, surface plasmon resonance (SPR) analysis confirmed direct binding of **T26** to FXR, with a moderate dissociation constant (K_d) of 13.8 μmol/L (Fig. S3D). These results suggest that **T26**, despite its limited FXR antagonism, serves as a promising starting point for the development of more potent bifunctional modulators (Fig. 2E).

2.2. *T26 binding mode prediction and molecular design*

Prior tostructural derivation, the binding modes of **T26** in both TGR5 and FXR were analyzed to inform rational optimization. While numerous active-state FXR structures are available, inactive-state FXR structures are limited to only two: ivermectin-bound FXR-corepressor complex (PDB ID: 4WVD)[51] and NDB-stabilized FXR homodimer (PDB ID: 4OIV)[52]. Given the high conformational flexibility of the FXR ligand-binding pocket (LBP), selecting the appropriate docking receptor model was essential. Ivermectin[51] exhibits dual functionality: it acts as an FXR antagonist by promoting co-repressor recruitment, while also displaying agonist-like behavior by enhancing FXR−SRC2 interaction. In contrast, both NDB[52] and **T26** function as pure antagonists. This pharmacological profile indicates that **T26** is more similar to NDB than with ivermectin. Therefore, the 4OIV structure was selected for induced-fit docking of **T26**, enabling a reliable prediction of its binding conformation and facilitating subsequent structure-based optimization.

As shown in Fig. 2D, **T26** adopts an L-shaped conformation within FXR LBP, with its Boc group extending deeply into a hydrophobic subpocket formed by helices H3, H5, and H6, while phenylethyl moiety interacts with H7. Dominant interactions are hydrophobic, except for a single hydrogen bond observed between the carbonyl group and His294 (Fig. 2B). The absence of additional polar interactions likely accounts for the relatively weak binding affinity observed in SPR assays. FXR activation requires ordered α12 helix for coactivator recruitment, whereas antagonism benefits from its disruption[53]. However, **T26** occupies a deep pocket, only contacting H112′ *via* its benzyl group, resulting in limited interaction and negligible antagonism. To improve FXR antagonism, we proposed adding substituents to enhance occupancy at functional pocket near H112' and disrupt coactivator binding.

To minimize the potential negative impacts of structural modifications on TGR5 agonism, we also predicted the binding mode of **T26** in TGR5 (Fig. 2C). **T26** adopts a reversed L-shape conformation, forming a key hydrogen bond with Tyr240. Additionally, the ethylbenzene moiety of **T26** engages in $\pi-\pi$ stacking with Tyr89, thereby contributing to the stabilization of the receptor's active conformation. Both Tyr240 and Tyr89 are critical in ligand recognition and allosteric signal propagation through TM3−TM6 dynamics, thus these interaction are critical and

should be preserved during structural optimization. Notably, the secondary benzylamine group of **T26**, which closes to H112′ in FXR and extends toward the extracellular region of TGR5, provides an accessible site for fragment extension.

2.3. General synthesis procedures

The synthesis of series A compounds is illustrated in Scheme 1. S_NAr addition of 1-Boc-piperazine to 2-fluorobenzaldehyde gave intermediate **2**. This intermediate then underwent reductive amination with 2-phenylethylamine to produce **T26**. Subsequently, the introduction of alkyl or acyl groups to form **A1**−**A3** was achieved through N-nucleophilic substitution. For compound **A3** with a carboxyl tail, additional ester hydrolysis was required.

The synthesis of sulfonamides **A4**−**A15** involved the preparation of corresponding sulfonyl chloride building blocks. Electron-rich benzenesulfonyl chlorides were readily obtained *via* direct chlorosulfonylation, while the sulfonyl chloride for **A13** was synthesized through a Buchwald-Hartwig coupling followed by oxidation of benzyl sulfide. Finally, the target sulfonamides were obtained through a DMAP-aided nucleophilic substitution and hydrolysis of the terminal ethyl ester.

As depicted in Scheme 2, compounds **B1**−**B14** were synthesized using similar routes, except that intermediate **6a** required a reduction step.

As illustrated in Scheme 3, the synthesis of series C compounds commenced with the construction of diverse secondary amines. These intermediates were obtained through nucleophilic substitution from a primary amine (**C1**), Buchwald-Hartwig coupling (**C2**), or reductive amination of substituted benzaldehydes (**C3**−**C10**). Subsequent sulfonamide formation and ester hydrolysis were performed as before.

For the synthesis of **D1**−**D7** (Scheme 4, upper), the intermediates **12a**−**12g** were prepared *via* S_NAr reaction of 2-fluorobenzaldehyde with various piperazine derivatives. For compounds **D8**−**D15** (Scheme 4, lower), the synthesis began with common intermediate **13**, derived from the de-Boc product of C8M. Diverse acyl substitutions were then introduced at the reactive site prior to ester hydrolysis.

Additionally, compounds **E4**−**E6** were synthesized *via* a convergent approach, starting with the preparation of intermediate E1M (Scheme 5). Different groups were subsequently introduced to replace the Boc protecting group.

2.4. Structure−activity relationship and binding pose analysis

We systematically investigated structure−activity relationships (SAR) by segmenting **T26** into four modifiable regions (Fig. 2E, region A−D). Guided by molecular docking analyses, Region A was identified as a suitable site for introducing new interactions to enhance FXR antagonism. And in TGR5 the secondary amine of **T26** is positioned within a hydrophobic subpocket surrounded by Trp75 and Phe161, while oriented toward the extracellular domain (Fig. 2C). This structural insight motivated the extension of region

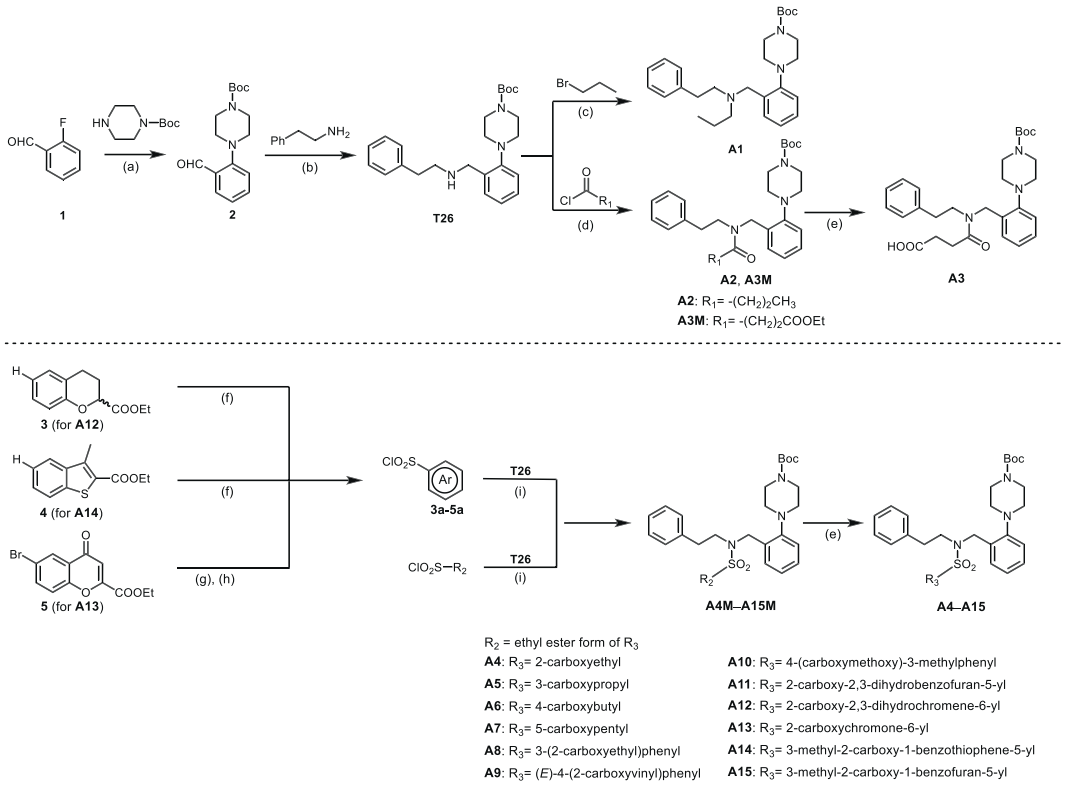

Scheme 1 Synthetic routes of series A compounds. Reagents and conditions: (a) K_2CO_3, dry DMF, 150 °C, 8 h, 79%; (b) Trimethyl orthoformate, $NaCNBH_3$, CH_3COOH, MeOH, N_2, 30 °C, 24 h, 66%; (c) KI, K_2CO_3, MeCN, 50 °C, 18 h, 82%; (d) DMAP, K_2CO_3, DMF, dry DCM, 0 °C to room temperature, 8 h, 79% to 93%; (e) LiOH, EtOH, H_2O, reflux for 1 h or room temperature for 18 to 24 h; then 2 N HCl adjusted to pH = 3, 21%−97%; (f) $ClSO_3H$, Chloroform, 0 °C to room temperature, 24 h, 23%−79%; (g) Benzyl thioalcohol, $Pd_2(dba)_3$, Xantphos, DIPEA, N_2, toluene, reflux, 18 h, 77%−84%; (h) *N*-Chlorosuccinimide, CH_3COOH, H_2O, room temperature, 3−10 h, 66%−84%; (i) DMAP, K_2CO_3, DMF, dry DCM, 50 °C, 24 h, 33%−48%.

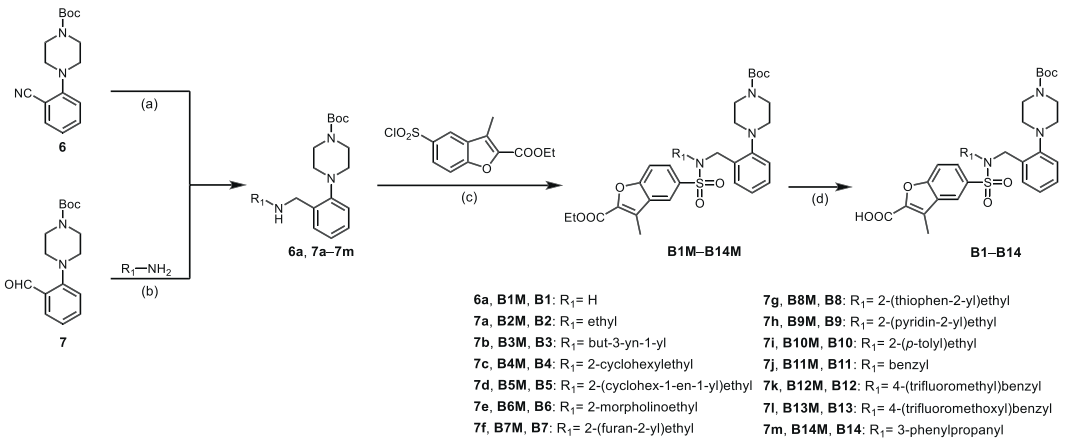

Scheme 2 Synthetic route of series B compounds. Reagents and conditions: (a) $NaBH_4$, trifluoroacetic acid, dry THF, 0 °C to room temperature, 48 h, 43%; (b) Trimethyl orthoformate, $NaCNBH_3$, CH_3COOH, MeOH, N_2, 30 °C, 24 h, 30%−98%; (c) DMAP, K_2CO_3, DMF, dry DCM, 50 °C, 24 h, 29%−82%; (d) LiOH, EtOH, H_2O, reflux, 1 h; then 2 N HCl adjusted to pH = 3, 49%−90%.

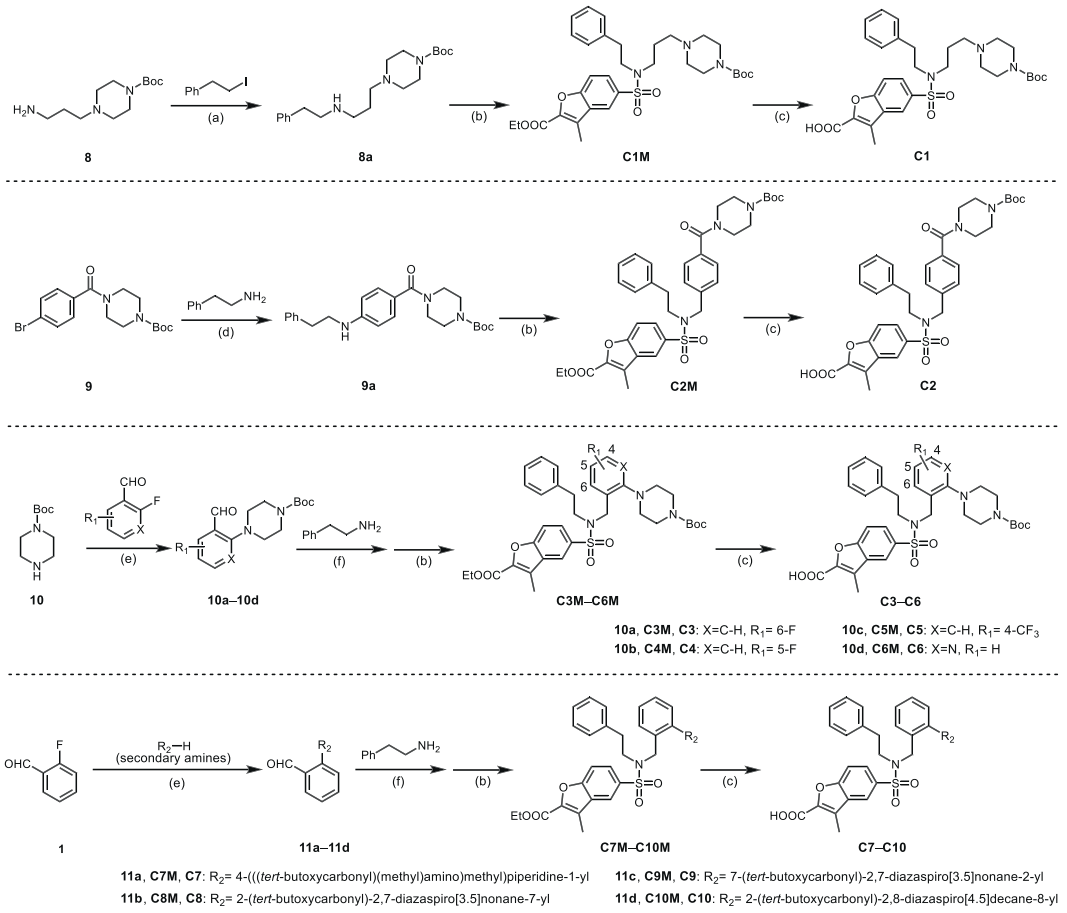

Scheme 3 Synthetic route of series C compounds. Reagents and conditions: (a) K_2CO_3, MeCN, 40 °C, 24 h, 91%; (b) Ethyl 5-(chlorosulfonyl)-3-methylbenzofuran-2-carboxylate, DMAP, K_2CO_3, DMF, dry DCM, 50 °C, 24 h, 32%−90%; (c) LiOH, EtOH, H_2O, reflux, 1 h; then 2 N HCl adjusted to pH = 3, 73%−96%; (d) $Pd_2(dba)_3$, BINAP, *t*-BuONa, N_2, toluene, 80 °C, 35 h, 86%; (e) K_2CO_3, dry DMF, 150 °C, 8 h, 11%−86%; (f) Trimethyl orthoformate, $NaCNBH_3$, CH_3COOH, MeOH, N_2, 30 °C, 24 h, 44%−88%.

A to introduce additional interactions with the extracellular loops of TGR5 and H112′ of FXR. Initial modifications showed that simple alkyl substitution (**A1**) failed to improve activity, whereas the introduction of polar group (**A2**) modestly enhanced FXR antagonism without significantly impairing TGR5 agonism (Table 1). Building upon this, we rationally designed derivatives featuring polar terminal groups and extended side chains to better occupy the solvent-accessible pocket present in both TGR5 and

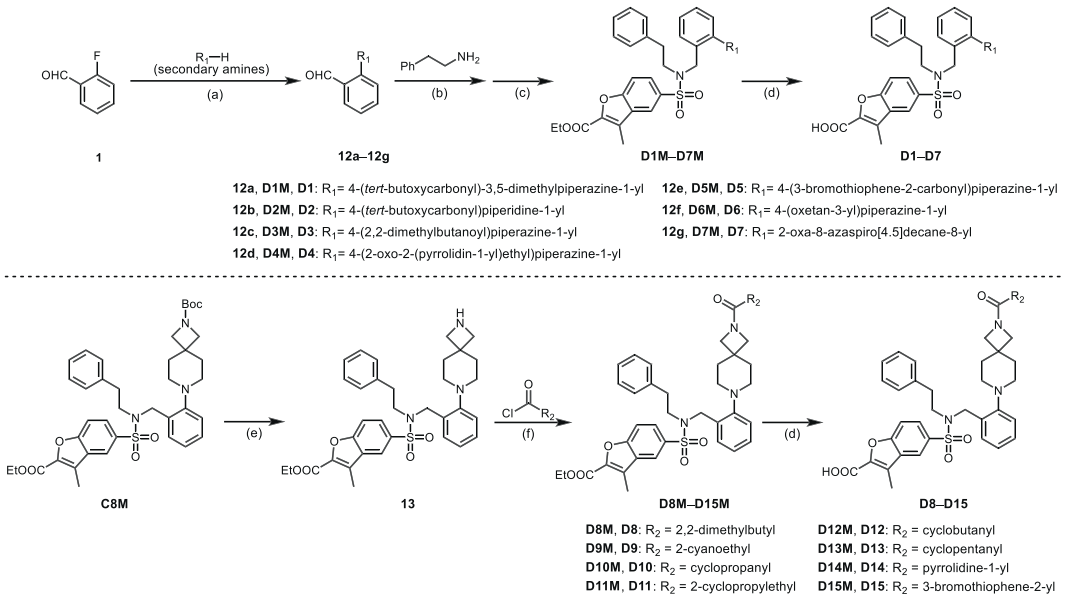

Scheme 4 Synthetic routes of series D compounds. Reagents and conditions: (a) K_2CO_3, dry DMF, 150 °C, 8 h, 39%−87%; (b) Trimethyl orthoformate, $NaCNBH_3$, CH_3COOH, MeOH, N_2, 30 °C, 24 h, 32%−82%; (c) Ethyl 5-(chlorosulfonyl)-3-methylbenzofuran-2-carboxylate, DMAP, K_2CO_3, DMF, dry DCM, 50 °C, 24 h, 46% −86%; (d) LiOH, EtOH, H_2O, reflux, 1 h; then 2 N HCl adjusted to pH = 3, 66% to 88%; (e) 2 N HCl, EA, room temperature, 2 h, 99%; (f) Triethylamine, dry DCM, N_2, 0 °C to room temperature, 18 h, 26%−83%.

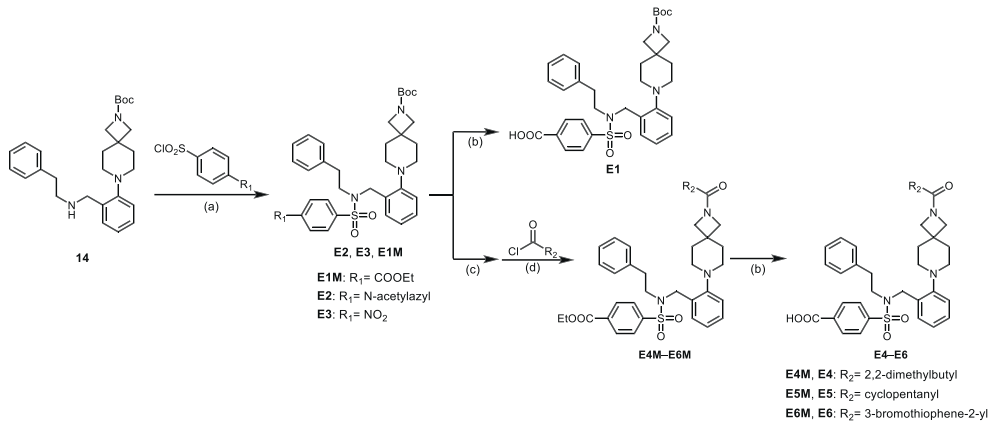

Scheme 5 Synthetic routed of series E compounds. Reagents and conditions: (a) DMAP, K_2CO_3, DMF, dry DCM, 50 °C, 24 h, 70%−81%. (b) LiOH, EtOH, H_2O, reflux, 1 h; then 2 N HCl adjusted to pH = 3, 54%−85%. (c) 2 N HCl, EA, room temperature, 2 h, 99%. (d) Triethylamine, dry DCM, N_2, 0 °C to room temperature, 18 h, 63%−78%.

FXR. Among these, compounds **A7** (bearing elongated flexible chain) and **A8** (with conformational restriction) showed markedly improved FXR inhibition while maintaining robust TGR5 activity. These results highlight that the importance of precise carboxyl group orientation in enhancing FXR antagonism while preserving TGR5 agonism. Subsequent investigation of *para*-carboxyl derivatives (Table 1) revealed that flexible linker incorporation (**A10**) outperformed rigid analog (**A9**). Additionally, ring-fused analogs featuring oxygen-containing conjugated scaffolds (**A11**−**A15**) provided further improvements in FXR inhibitory activity, demonstrating the potential of scaffold modulation in optimizing dual-target engagement.

Modifications in Region B were initiated by replacing original phenethyl group (Table 2). Since the phenyl group in compound **A15** faced Phe161 in TGR5 (Supporting Information Fig. S4A), a series of hydrophobic and electronically diverse surrogates were synthesized to evaluate the contribution of hydrophobic and $\pi-\pi$ interactions. Deletion of the phenyl ring (**B1**) completely abolished FXR antagonism, although it moderately enhanced TGR5 agonistic activity. Hydrophobic and flexible substituents (**B2**, **B4**, **B5**) largely maintained FXR antagonistic activity, whereas incorporation of a linear alkynyl group (**B3**) reduced potency. Notably, the introduction of an ionizable morpholine moiety (**B6**) abrogated FXR inhibition entirely. Electron-rich aryl substitutions (**B7**−**B10**) proved optimal for FXR activity, while variation in linker-length (**B11**−**B14**) did not yield significant improvements. Interestingly, TGR5 showed an opposing preference at this position, favoring polar substituents such as those in **B6** and **B9**. Although **B8** exhibited potent dual activity against both TGR5 and FXR, its dominant fragment was not retained due to metabolic

Table 1 TGR5 and FXR activities of **T26** derivatives with modifications at region A (**A1**−**A15**).

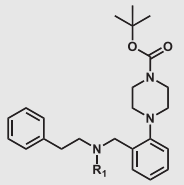

Compd.	R_1	hTGR5 agonism[a]		FXR antagonism[b]
		EC_{50} (μmol/L)	E_{max} (%INT777)	Antagonistic rate% at 5 μmol/L
INT-777	–	0.2 ± 0.02	100	N.D.[c]
Z&E-Guggulsterone	–	N.D.	N.D.	73.8 at 50 μmol/L
T26 (hit)	H	2.5 ± 0.2	57.1	31.3 at 50 μmol/L (IC_{50} = 115.0 ± 44.5 μmol/L)
A1		5.4 ± 2.5	75.7	0.3
A2		3.2 ± 0.8	71.0	9.7
A3	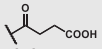	6.0 ± 1.2	74.4	10.3
A4	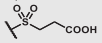	4.6 ± 1.1	73.8	10.3
A5	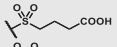	11.7 ± 5.9	81.4	23.0
A6	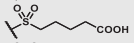	2.8 ± 1.4	73.0	16.0
A7	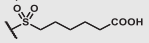	2.8 ± 0.4	70.3	42.1
A8	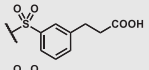	2.6 ± 0.3	58.7	49.3
A9	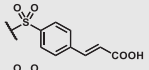	9.2 ± 4.3	59.7	28.1
A10	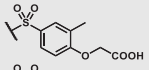	5.2 ± 0.8	55.4	60.6
A11	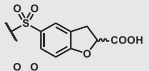	3.1 ± 0.5	61.0	38.0
A12	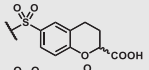	2.7 ± 0.3	58.9	43.4
A13	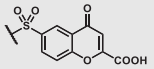	3.7 ± 0.6	63.3	68.8
A14	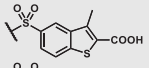	2.6 ± 0.3	57.5	49.9
A15	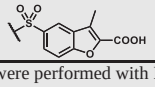	3.4 ± 0.4	61.1	61.8

[a]Control assays were performed with INT-777. EC_{50} values were determined in triplicate (n = 3) and are presented as mean ± the standard error of the mean (SEM). E_{max} values were determined in triplicate (n = 3) and are presented as mean relative activation, calculated by comparison to the maximum efficacy of INT-777 (set as 100%). [b] Control assays were performed with 50 μmol/L CDCA alone and in combination with 50 μmol/L *Z*&*E*-guggulsterone. The antagonistic rates were calculated as 100% × ([Compd–DMSO]/[CDCA–DMSO]) and are represented as the mean of quadruplicate determinations (n = 4). Relative IC_{50} values were determined in quadruplicate (n = 4) and are represented as mean ± SEM. [c] N.D. indicates "not determined".

stability concerns, as the unsubstituted, electron-rich thiophene moiety is highly susceptible to metabolic oxidation, including S-oxidation and epoxidation[54]. To reconcile the divergent structural preferences of the two targets and preserve dual activity, we retained the phenyl group in Region B as a structural compromise.

The exploration of Region C (Table 3) began by modifying phenyl (**C1**−**C6**) while maintaining the 1-Boc-piperazine moiety. The results showed that a flexible linker (**C1**) abolished FXR antagonism, whereas the para-piperazine analog (**C2**) reduced activity toward both targets. Given the proximity of the phenyl group in region C to the backbone of Tyr89 (Fig. S4B−S4D), we introduced substituents to engage additional interactions. Electron-withdrawing groups or reduced electron density (**C3**−**C6**) weakened TGR5 agonism without improving FXR antagonism. Compound **C6** showed a modest 1.2-fold improvement in TGR5 agonism compared to **A15**, but exhibited reduced FXR antagonism. Further exploration involved expanding the piperazine core, yielding an extended alkyl derivatives (**C7**) and spirocyclic analogs (**C8**−**C10**). A distinct steric preference was unveiled: smaller Boc-side hindrance (**C8**) enhanced activity for both targets, while its reversed analog (**C9**) were detrimental. Based on this SAR, both the parent piperazine and the optimized spirocyclic derivative **C8** were selected for further development.

Table 2 TGR5 and FXR activities of **A15** derivatives with modifications at region B (**B1**−**B14**).

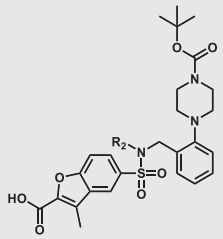

Compd.	R_2	hTGR5 agonism[a]		FXR antagonism[b]
		EC_{50} (μmol/L)	E_{max} (%INT-777)	Antagonistic rate% at 5 μmol/L (IC_{50}, μmol/L)
B1	H	2.9 ± 1.9	78.8	7.2
B2		4.8 ± 2.1	75.6	68.6
B3		13.4 ± 6.7	61.1	25.9
B4		15.0 ± 7.0	63.0	65.5 (3.1 ± 0.7 μmol/L)
B5		6.6 ± 2.5	72.9	68.5
B6		3.0 ± 0.3	61.0	0
B7		3.7 ± 0.5	62.8	71.2
B8		3.3 ± 0.6	64.4	73.6 (1.7 ± 0.3 μmol/L)
B9		2.8 ± 0.3	58.0	45.5
B10	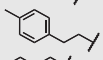	4.4 ± 1.4	58.1	56.8
B11		7.9 ± 1.8	62.9	51.8
B12	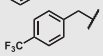	10.0 ± 3.7	64.7	43.5
B13	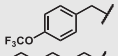	14.9 ± 9.3	63.8	37.0
B14	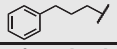	4.4 ± 1.2	68.8	54.8

[a]Control assays were performed with INT-777. EC_{50} values were determined in triplicate (n = 3) and are presented as mean ± the standard error of the mean (SEM). E_{max} values were determined in triplicate (n = 3) and are presented as mean relative activation, calculated by comparison to the maximum efficacy of INT-777 (set as 100%). [b] Control assays were performed with 50 μmol/L CDCA alone and in combination with 50 μmol/L *Z*&*E*-guggulsterone. The antagonistic rates were calculated as 100% × ([Compd–DMSO]/[CDCA–DMSO]) and are represented as the mean of quadruplicate determinations (n = 4). Relative IC_{50} values were determined in quadruplicate (n = 4) and are represented as mean ± SEM.

Since the Boc group is essential for TGR5 agonistic efficacy, as evidenced by the reduced efficacy of the deprotected compound **D2-**deBoc compared to **D2**, and forms a hydrogen bond interation with Tyr240 (Fig. S4E), yet is susceptible to acidic hydrolysis under oral administration, we pursued modifications in Region D (Table 4) to enhance hydrolytic stability *via* two main strategies: hydrolysis-protective substitutions (**D1**, **D2**) and entire Boc replacement with linear or cyclic substituents (**D3**−**D15**). Introducing steric hindrance (**D1**) mildly increased FXR antagonism but negatively affected TGR5 agonism, while amide replacement (**D2**) led to reduced activity against both targets. Boc replacement with sterically hindered alkyl groups (**D3**, **D8**) increased FXR antagonism, whereas unbranched chain (**D9**) decreased activity across both targets. Encouraged by these results, we further introduced cyclic substituents to enhance van der Waals interactions while maintaining hydrogen bond acceptor capability. In the FXR binding site, aromatic (**D5**, **D15**) and alkyl groups (**D7**, **D10**−**D13**) outperformed amine analogs (**D4**, **D14**), suggesting a predominantly hydrophobic environment. In the corresponding TGR5 pocket, both sterically bulky and planar groups were tolerated, though linker elongation (**D11**) proved detrimental to activity.

To improve compound solubility and facilitate subsequent *in vitro* and *in vivo* activity evaluation, molecular planarity was reduced and lipophilicity was lowered by decreasing the calculated log*P* (*c*log*P*) values (Table 5). SAR and molecular docking studies of **C8** analogs (**E1**−**E3**) demonstrated that hydrogen bond donors are essential for maintaining dual-target potency (Fig. S4G). Building on this insight, optimized Boc surrogates (**D8**, **D13**, **D15**) were incorporated into the benzoic acid-based scaffold (**E1**), resulting in enhanced modulators **E4**−**E6**. These compounds exhibited both reduced *c*log*P* values and enhanced FXR binding affinity, with K_D values improving from 13.8 (**T26**) to 0.73 (**E4**), 1.78 (**E5**), and 1.15 μmol/L (**E6**) (Fig. S3).

Through five rounds of iterative optimization (A−D regions) on **T26**, we developed bifunctional modulators with enhanced FXR antagonism. Their bidirectional SAR is presented in Fig. 3A.

Table 3 TGR5 and FXR activities of **A15** derivatives with modifications at region C (**C1**−**C10**).

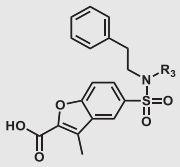

Compd.	R_3	hTGR5 agonism[a]		FXR antagonism[b]
		EC_{50} (μmol/L)	E_{max} (%INT-777)	Antagonistic rate% at 5 μmol/L (IC_{50}, μmol/L)
C1	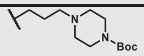	5.4 ± 1.4	68.6	0
C2	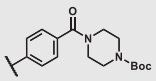	13.5 ± 4.7	62.5	19.2
C3	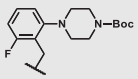	8.1 ± 2.7	61.2	53.3
C4	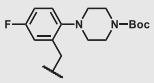	10.3 ± 5.4	60.7	55.6
C5	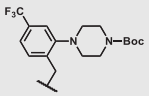	18.4 ± 13.6	70.7	27.5
C6	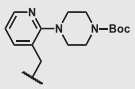	2.8 ± 0.3	59.5	50.8
C7	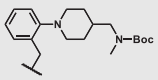	5.4 ± 3.5	71.2	76.2
C8	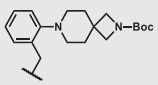	2.7 ± 0.3	60.5	76.6 (1.3 ± 0.4 μmol/L)
C9	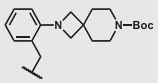	9.7 ± 3.6	73.2	15.5
C10	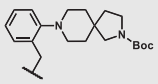	3.1 ± 0.3	60.4	78.5 (3.6 ± 0.5 μmol/L)

[a]Control assays were performed with INT-777. EC_{50} values were determined in triplicate (n = 3) and are presented as mean ± the standard error of the mean (SEM). Emax values were determined in triplicate (n = 3) and are presented as mean relative activation, calculated by comparison to the maximum efficacy of INT-777 (set as 100%). [b]Control assays were performed with 50 μmol/L CDCA alone and in combination with 50 μmol/L *Z*&*E*-guggulsterone. The antagonistic rates were calculated as 100% × ([Compd–DMSO]/[CDCA–DMSO]) and are represented as the mean of quadruplicate determinations (n = 4). Relative IC_{50} values were determined in quadruplicate (n = 4) and are represented as mean ± SEM.

For Region A modifications, extension of the hydrophobic linker coupled with polar tail incorporation significantly enhanced FXR antagonism. Subsequent refinement of the spiral C-heterocycle produced **C8**, demonstrating improved FXR antagonism (IC_{50} = 1.3 μmol/L) and enhanced TGR5 agonism (EC_{50} = 2.7 μmol/L, E_{max} = 60.5%). Strategic replacement of the Boc group in the Region D with steric (**D8**), twisted (**D13**), or planar (**D15**) moieties preserved dual activity while addressing hydrolysis liability. Finally, planarity reduction in the A-region improved *c*log*P*, yielding **E4**−**E6** with maintained potent dual activity across both targets (EC_{50}/IC_{50} = 1−5 μmol/L). Molecular docking poses of representative compounds were analyzed (Fig. S4), providing structural insights into differential ligand−receptor interactions and supporting the rational design strategy.

As a nuclear transcription factor, FXR mediates downstream gene expression. To evaluate the functional modulation of FXR by our compounds, dual-luciferase reporter assays were performed with compounds **E4**, **E5**,and **E6**. All three compounds effectively suppressed CDCA-induced transcriptional activity in FXR-overexpressing HEK293T cells without inhibiting cell

Table 4 TGR5 and FXR activities of **A15/C8** derivatives with modifications at region D (**D1**−**D15**).

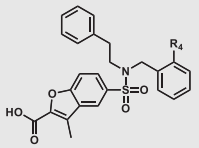

Compd.	R_4	hTGR5 agonism[a]		FXR antagonism[b]
		EC_{50} (μmol/L)	E_{max} (%INT-777)	Antagonistic rate% at 5 μmol/L (IC_{50}, μmol/L)
D1	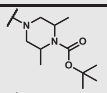	15.8 ± 7.3	68.8	73.5 (2.2 ± 0.3 μmol/L)
D2	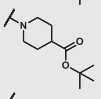	17.0 ± 3.7	63.0	43.4
D2-deBoc		15.2 ± 1.2	46.9	(4.75 ± 0.22 μmol/L)
D3		2.1 ± 0.8	66.4	64.1 (2.3 ± 0.5 μmol/L)
D4	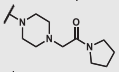	6.4 ± 5.9	73.8	28.1
D5		5.9 ± 2.4	73.7	73.6
D6		5.8 ± 2.5	67.6	2.2
D7		5.7 ± 3.4	71.4	58.9
D8	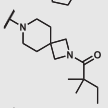	7.2 ± 5.9	75.1	100 (2.3 ± 1.3 μmol/L)
D9	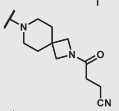	8.3 ± 5.6	70.3	23.7
D10	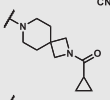	4.3 ± 1.3	71.2	60.9
D11	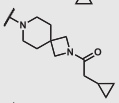	15.2 ± 14.0	80.8	65.3
D12	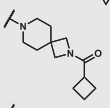	5.4 ± 2.5	70.5	83.3 (1.5 ± 0.3 μmol/L)
D13	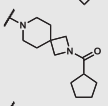	7.5 ± 4.3	77.4	83.9 (2.6 ± 0.8 μmol/L)
D14	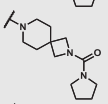	9.9 ± 4.9	73.6	30.7
D15	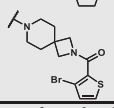	5.4 ± 2.0	72.5	81.7 (1.3 ± 0.4 μmol/L)

[a]Control assays were performed with INT-777. EC_{50} values were determined in triplicate (n = 3) and are presented as mean ± the standard error of the mean (SEM). E_{max} values were determined in triplicate (n = 3) and are presented as mean relative activation, calculated by comparison to the maximum efficacy of INT-777 (set as 100%). [b] Control assays were performed with 50 μmol/L CDCA alone and in combination with 50 μmol/L *Z*&*E*-guggulsterone. The antagonistic rates were calculated as 100% × ([Compd–DMSO]/[CDCA–DMSO]) and are represented as the mean of quadruplicate determinations (n = 4). Relative IC_{50} values were determined in quadruplicate (n = 4) and are represented as mean ± SEM.

Table 5 Potency and *c*log*P* of polar tail derivatives **E1**−**E6**.

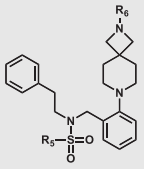

Compd.	R_5	R_6	*c*log*P*[a] (parent)	hTGR5 agonism[b]		FXR antagonism[c]
				EC_{50} (μmol/L)	E_{max} (%INT-777)	Relative IC_{50} (μmol/L)
E1		Boc	5.08 (5.71)	3.0 ± 1.0	71.9	5.1 ± 1.6
E2	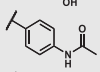	Boc	4.87 (5.71)	3.7 ± 1.7	73.0	5.4 ± 1.4
E3		Boc	5.45 (5.71)	4.3 ± 1.0	72.0	0.7%[d]
E4			5.23 (5.68)	5.1 ± 2.3	75.9	5.1 ± 1.5
E5			4.22 (5.02)	3.6 ± 0.8	71.2	2.3 ± 0.7
E6			4.91 (5.49)	2.4 ± 0.4	66.6	1.3 ± 0.1

[a]Data were calculated using the ADMElab 3.0 web service. Calculated log*P* values are presented for each derivative (with the parent compound value in parentheses). [b] Control assays were performed with INT-777. EC_{50} values were determined in triplicate (n = 3) and are presented as mean ±standard error of the mean (SEM). E_{max} values were determined in triplicate (n = 3) and are presented as mean relative activation, calculated by comparison to the maximum efficacy of INT-777 (set as 100%). [c] Control assays were performed with 50 μmol/L CDCA alone and in combination with 50 μmol/L *Z*&*E*-guggulsterone. The antagonistic rates were calculated as 100% × ([Compd–DMSO]/[CDCA–DMSO]) and are represented as the mean of quadruplicate determinations (n = 4). Relative IC_{50} values were determined in quadruplicate (n = 4) and are represented as mean ± SEM. [d] The antagonistic rate was measured at 5 μmol/L. The result represents the mean of quadruplicate determinations (n = 4).

proliferation (Supporting Information Fig. S6A−S6C), confirming their role as potent functional antagonists (Fig. 3B−D). Notably, **E4** and **E6** exhibited significant inhibitory activity even at submicromolar concentrations, with IC_{50} values of 3.8 and 2.8 μmol/L, respectively.

To elucidate SAR and binding patterns underlying bifunctional modulator preferences, 50-ns molecular dynamics (MD) simulations were conducted to examine ligand binding within TGR5 and FXR (Supporting Information Fig. S5). Using **E6** as a representative scaffold, the simulations revealed **E6** occupies a position higher than **T26** in the TGR5 binding pocket (Fig. 4A), with its benzoic acid moiety extending toward extracellular domain (ECD) while maintaining key interactions within transmembrane pocket. Beyond conserved contacts, **E6** potentially enhances activation through $\pi-\pi$ stacking between 2-bromothienoformyl and Tyr240, correlating with the observed increase in efficacy. Notably, the $\pi-\pi$ stacking with Tyr89 shifts from Region B in **T26** to Region C in **E6** (Fig. 4B), providing a rationale for the retained TGR5 agonism despite phenyl removal in region B modifications (Table 2, **B1** and **B2**). In FXR (Fig. 4C), **E6** demonstrates superior occupancy, maintaining stable interactions with Phe329, Ser332, Tyr369, His445, His447, Ala448, Leu451 throughout the MD simulation (Fig. S5D). The sulfonyl benzoic acid group establishes three polar contacts (with Ser332 and His445) and a $\pi-\pi$ interaction with Phe329 (Fig. 4D). The structural elements introduced in region A and region B collectively restrict the positioning of H112′ (residues Asn444−Met452; Fig. S5D) and effectively seal the LBP, thereby impairing α12 helix ordering and impairing coactivator recruitment.

2.5. Protective effects of bifunctional modulators on cardiomyocytes exposed to hypoxia/reoxygenation (H/R)

The cytotoxicity profiles of three modified compounds (**E4**−**E6**, Fig. S6D−S6F) were evaluated in cardiomyocytes, and the pharmacological effects of these compounds (**E4**−**E6**) and their common precursor (**C8**) were assessed in hypoxia/reoxygenation (H/R) models. Cardiomyocytes were subjected to 18 h of hypoxia followed by 6 h of reoxygenation, with continuous compound treatment throughout the 24-h period. Initial screening in rat

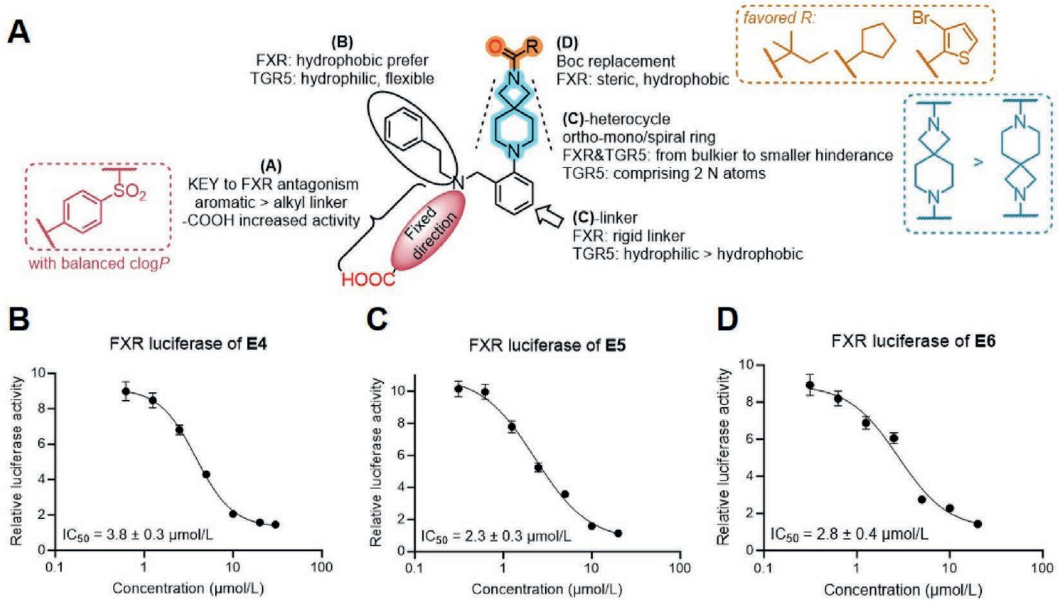

Figure 3 Target SAR and luciferase activity of compound structural optimization. (A) Summary of SAR studies for **T26** derivatives. (B−D) FXR antagonistic activity of compounds **E4**, **E5**, and **E6** measured by cell-based dual-luciferase reporter assays.

(H9c2) and human (AC16) cardiomyocyte cell lines revealed **E4** and **E6** significantly improved viability post-H/R injury (Fig. 5A and B), prompting further evaluation in neonatal mouse cardiomyocytes (NMCMs). Ursodeoxycholic acid (UDCA), an endogenous bile acid with bidirectional TGR5/FXR modulatory activity[55,56] serving as a positive control[57,58]. Notably, **E4** and **E6** provided superior protection for NMCMs against H/R insults at substantially lower concentrations than UDCA (Fig. 5C).

To further evaluate the cardioprotective effects of E6, we assessed its anti-apoptotic activity in H/R-injured NMCMs using Annexin V/PI flow cytometry and TUNEL staining. Flow cytometry analysis revealed that 2 μmol/L **E6** did not significantly affect early apoptosis under H/R conditions (Annexin V^+/PI^-, Fig. 6A and B), but significantly reduced late apoptotic cells (Annexin V^+/PI^+, $P < 0.01$, Fig. 6C). Consistently, TUNEL staining demonstrated that **E6** markedly reduced the apoptotic rate of NMCMs exposed to H/R injury ($P < 0.0001$, Fig. 6D and E).

MIRI involves a multifactorial pathophysiological cascade, including oxidative stress, inflammatory responses, calcium overload, and various forms of cardiomyocyte death through necrosis, apoptosis and so on[6,59]. Reactive oxygen species (ROS) are key mediators of MIRI, initiating oxidative damage and amplifying cellular injury[60,61]. Both TGR5[24] and FXR[33] have been implicated in mitigating ROS-related damage and contributing to myocardial protection. DCFH-DA staining (Supporting Information Fig. S7A) revealed a substantial increase in intracellular ROS levels following H/R insult, which was significantly attenuated by treatment with 50 μmol/L UDCA or 5−10 μmol/L of either **E4** or **E6** (Fig. 7A). Furthermore, H/R led to elevated mitochondrial ROS levels, triggering mitochondrial permeability transition pore (mPTP) opening and subsequent dysfunction. MitoSOX Red assays (Fig. S7B) confirmed that **E4** and **E6** markedly suppressed mitochondrial ROS accumulation (Fig. 7B). In light of these results, bifunctional modulators **E4** and **E6** confer protective effects in H/R-induced cardiomyocyte injury, primarily through attenuation of oxidative stress. Among them, **E6** showed superior efficacy in reducing both cell death and ROS overproduction, making it a strong candidate for subsequent *in vivo* investigation.

2.6. *Safety and PK profiles of* ***E6***

A 7-day repeat dose toxicology study was conducted to evaluate the safety profile of compound **E6** in male C57BL/6 mice administered orally at doses of 100 and 150 mg/kg/day. Throughout the study period, all mice survived without abnormal behaviors or significant changes in body weight (Fig. 8A). Postmortem analysis showed no significant alterations in organ weights (Fig. 8D−G), histopathological examination by hematoxylin and eosin (HE) staining indicated normal tissue architecture across major organs (Fig. 8P). Biochemical assessments further confirmed unaltered hepatic and renal function, with serum markers remaining within physiological ranges (Fig. 8H−K). Cardiac function was evaluated *via* transthoracic echocardiography (Fig. 8L−O and 8Q), and revealed regular heart rate, normal left ventricular diastolic volume (LV Vol-d), and preserved systolic function, as indicated by stable left ventricular ejection fraction (LVEF) and fractional shortening (LVFS) values. Collectively, these findings suggest that E6 is well-tolerated at the tested doses and does not elicit overt toxicity in major organs, including the heart. TGR5 agonist are known to induce gallbladder enlargement through bile accumulation with impaired efflux[62]. FXR antagonism may counteract this effect *via* two complementary mechanisms: relieving FGF15-mediated suppression of cholecystokinin[63], and decreasing bile formation by downregulation of canalicular transporters[64]. In our experiments, 7-day oral administration of **E6** resulted in gallbladder length and width comparable to those of vehicle-treated controls (Fig. 8B−C), indicating no evidence of gallbladder enlargement. These findings further support the oral safety of **E6** in subacute toxicity assessment.

Prior to *in vivo* pharmacological evaluation, the pharmacokinetic profile **E6** was assessed in male mice following intravenous (1 mg/kg) or oral (10 mg/kg) administration (Table 6). Plasma

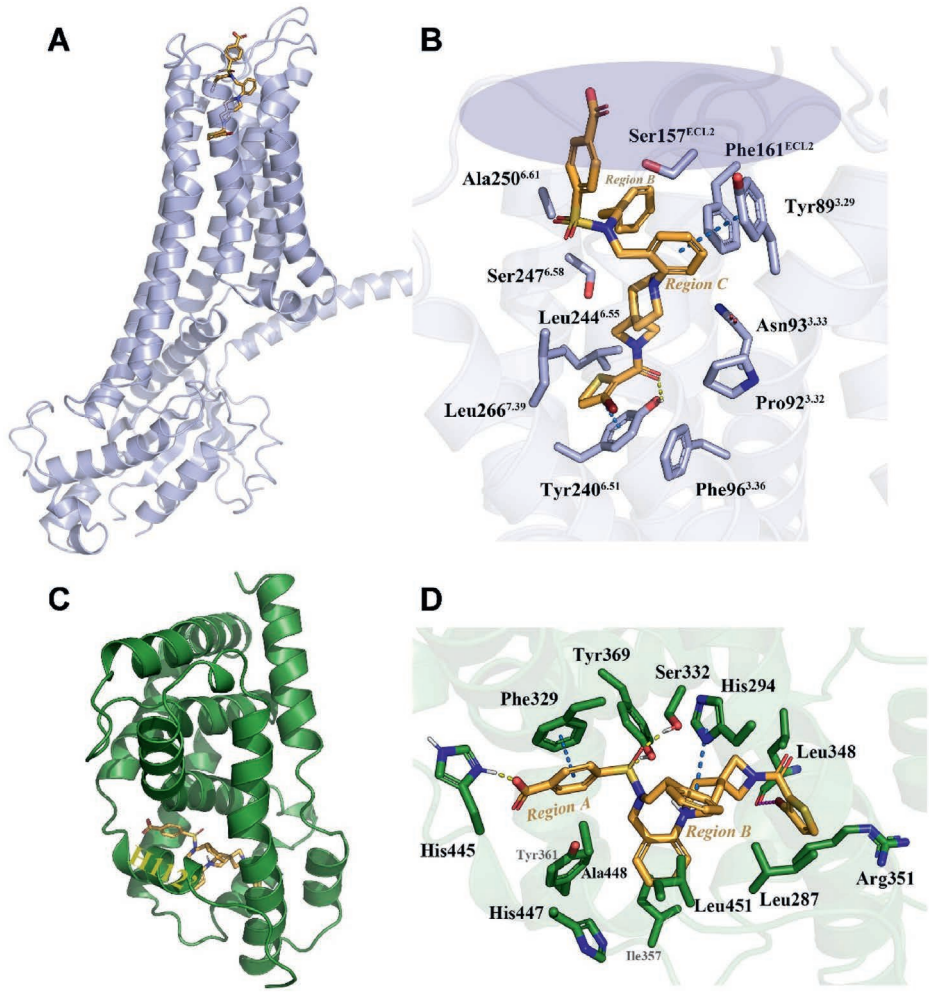

Figure 4 Overall and detailed binding poses of **E6** (orange) in the TGR5 orthosteric pocket (purple, A and B) or FXR LBP (green, C and D) from 50-ns molecular dynamics simulation. (B) The shaded area represents the extracellular domain of TGR5. (C) Regions A and B of **E6** collectively constrain the positioning of H112′. Yellow dashed lines indicate hydrogen bonds, fuchsia dashed lines indicate halogen bond, and blue dashed lines indicate $\pi-\pi$ stacking interactions.

concentrations of **E6** peaked rapidly after dosing in both routes, followed by a gradual decline (Supporting Information Fig. S8). Pharmacokinetic analysis demonstrated moderate oral bioavailability of 38% and a half-life ($t_{1/2}$) of 1.20 h. Considering its adequate oral bioavailability and relatively rapid systemic clearance, a higher oral dose was selected for subsequent cardiac I/R studies to ensure sufficient exposure.

2.7. *In vivo efficacy of **E6** against MIRI*

Compound **E6** was evaluated in a murine model of MIRI, involving 30 min of left anterior descending coronary artery occlusion followed by 24 h of reperfusion. Male C57BL/6 mice were pretreated orally for three consecutive days with **E6** (10 or 50 mg/kg/day), UDCA (50 mg/kg/day, as positive control), or vehicle prior to ischemia induction (Fig. 9A). After reperfusion, cardiac systolic function was quantified as LVEF and LVFS by echocardiography. Surgical consistency was determined by calculating the area at risk relative to the left ventricle (AAR/LV), while infarct size was expressed as ratio of infarct area to AAR (IF/AAR).

Following I/R procedures, the control group exhibited averaged infarct size of 45.75% relative to the AAR, while treatment with 50 mg/kg UDCA reduced infarct size to 20.59%. Notably, **E6** treatment resulted in dose-dependent reductions, with infarct sizes of 27.68% at 10 mg/kg, and 20.29% at 50 mg/kg (Fig. 9E–G). **E6** showed strong effect in enhancing systolic function (Fig. 9B–D). In LVEF measurements (Figs. 9C), 50 mg/kg UDCA improved LVEF to 56.38%, while **E6** improved it to 61.34% (10 mg/kg) and 63.67% (50 mg/kg), respectively. Parallel enhancement was observed in LVFS (50 mg/kg UDCA: 30.23%, **E6**: 30.95% at 10 mg/kg and 32.77% at 50 mg/kg (Fig. 9D).

2.8. *Clinical therapeutic potential of **E6***

To further investigate the therapeutic potential of **E6**, we measured serum levels of cardiac troponin T (cTnT) and troponin I (cTnI), clinically established markers of myocardial injury, 24 h after reperfusion. Treatment with **E6** at 50 mg/kg/day for three days significantly reduced both cTnT ($P < 0.05$, Fig. 10A) and cTnI ($P < 0.01$, Fig. 10B), indicating a protective effect against myocardial damage. Consistently, TUNEL staining of heart tissues demonstrated that **E6** markedly attenuated cardiomyocyte apoptosis during ischemia–reperfusion injury ($P < 0.05$, Fig. 10C–D), further supporting its cardioprotective efficacy *in vivo*.

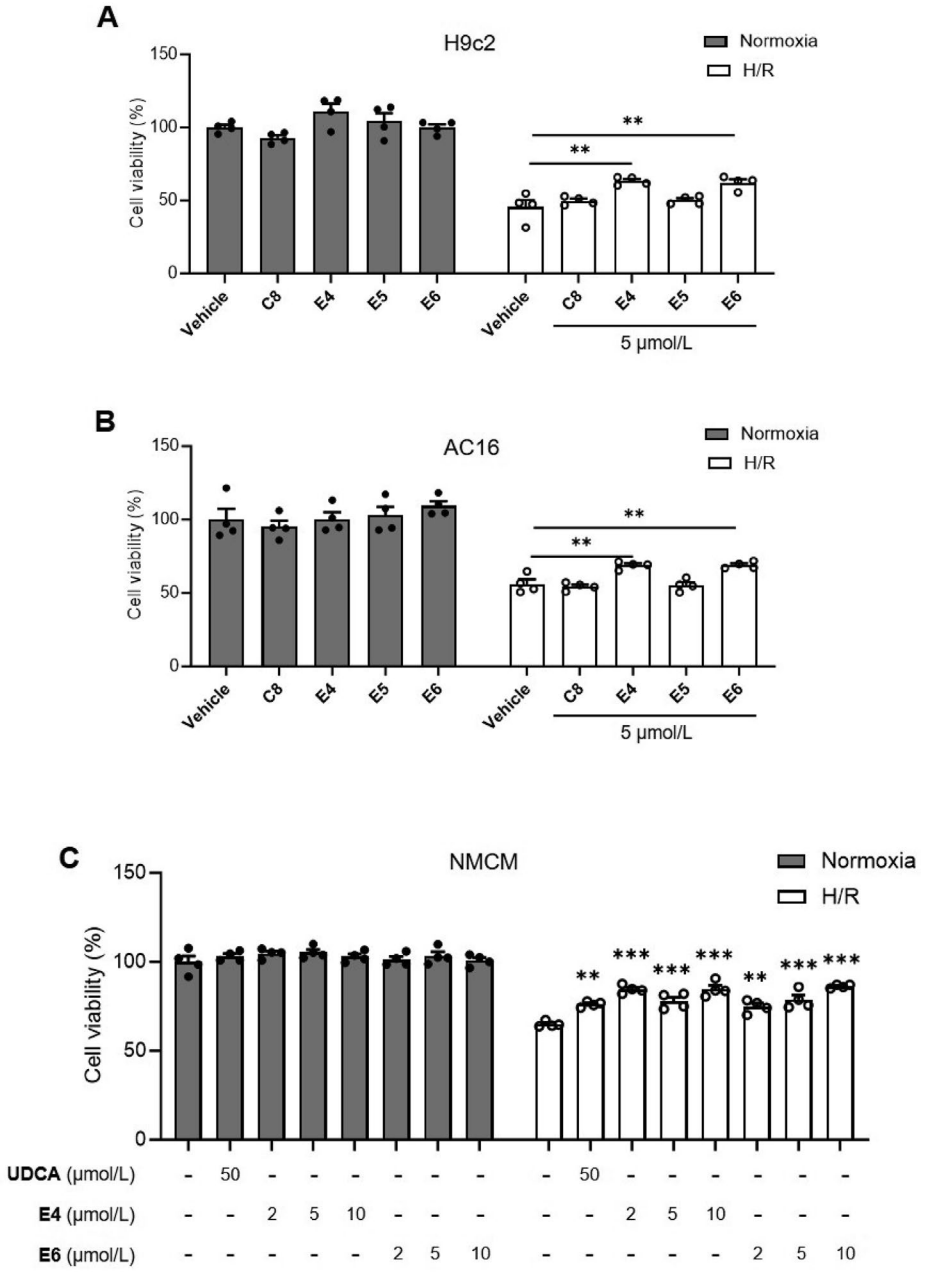

Figure 5 Effects of indicated compounds on cell viability in cardiomyocytes exposed to hypoxia/reoxygenation (H/R). Cell viability was evaluated using the CCK-8 assay. (A) H9c2 cells (rat myocardial cell line). (B) AC16 cells (human cardiac cell line). (C) NMCMs (neonatal mouse cardiomyocytes). Results are presented as mean ± SEM ($n = 4$). $^{**}P < 0.01$ *vs.* H/R vehicle control; $^{***}P < 0.001$, *vs.* H/R vehicle control.

Inflammation is a hallmark of MIRI, characterized by temporally dynamic immune cell recruitment and cytokine release. To further delineate the inflammatory response, we assessed immune cell infiltration and cytokine expression in ischemic heart tissue. In the MIRI model, infiltration of F4/80$^+$ macrophages was significantly increased ($P < 0.05$, Supporting Information Fig. S9C and S9D), whereas CD3$^+$ T cell counts remained unchanged (Fig. S9A and S9B). E6 treatment did not significantly affect the recruitment of either cell population. In contrast, E6 administration markedly suppressed the expression of multiple proinflammatory cytokines, including IL-1β, IL-2, IL-5, IL-6, IL-12p70, IL-17F, IL-21, IL-23p19, TNF-α, and IFN-γ (Supporting Information Fig. S10). These findings indicate that E6 attenuates acute inflammatory overactivation by dampening cytokine release rather than modulating immune cell infiltration. Collectively, this anti-inflammatory effect likely contributes to its ability to attenuate cardiomyocyte apoptosis and limit tissue damage in MIRI.

2.9. *Therapeutic advantages of bidirectional modulators*

To elucidate the downstream molecular effects of **E6** on FXR and TGR5 signaling pathways, Western blot analysis was conducted in NMCMs. The bifunctional modulator **E6**, significantly upregulated

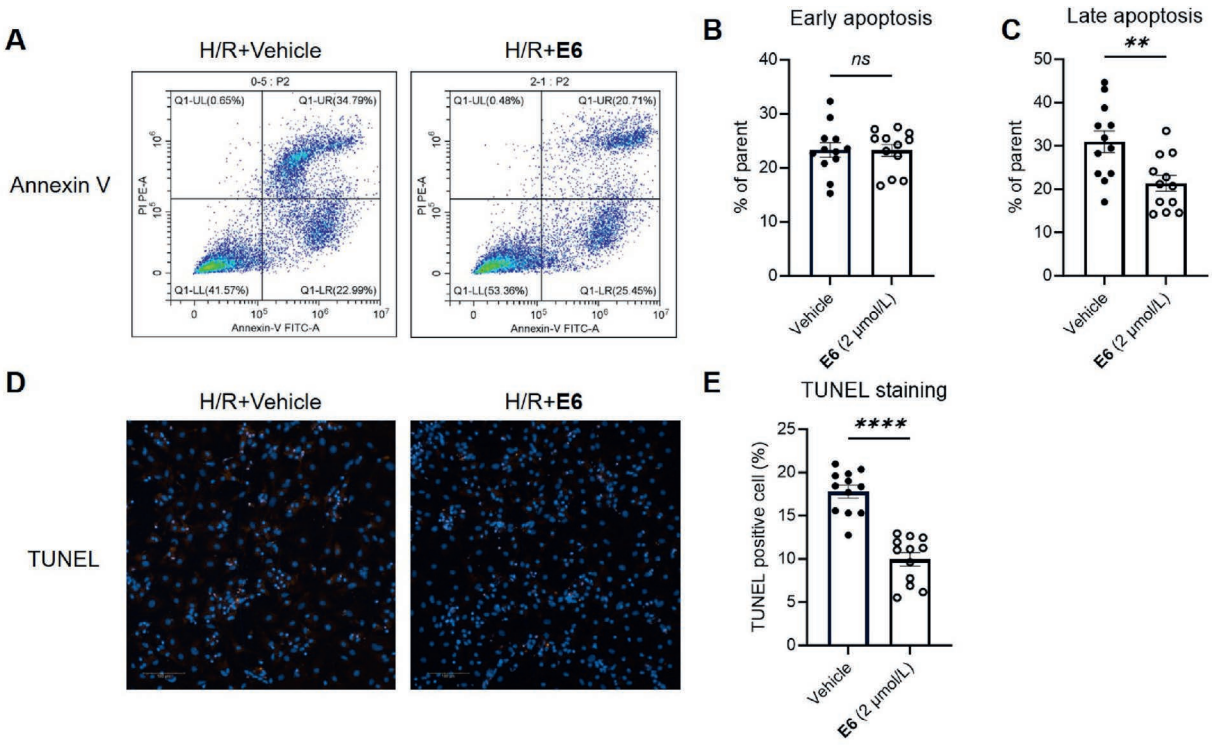

Figure 6 Effects of **E6** on apoptosis in NMCMs under H/R conditions. Apoptosis was assessed by Annexin V/PI flow cytometry (A−C) and TUNEL staining (D−E). Results are presented as mean ± SEM ($n = 12$). $^{**}P < 0.01$, $^{****}P < 0.0001$, ns: not significant.

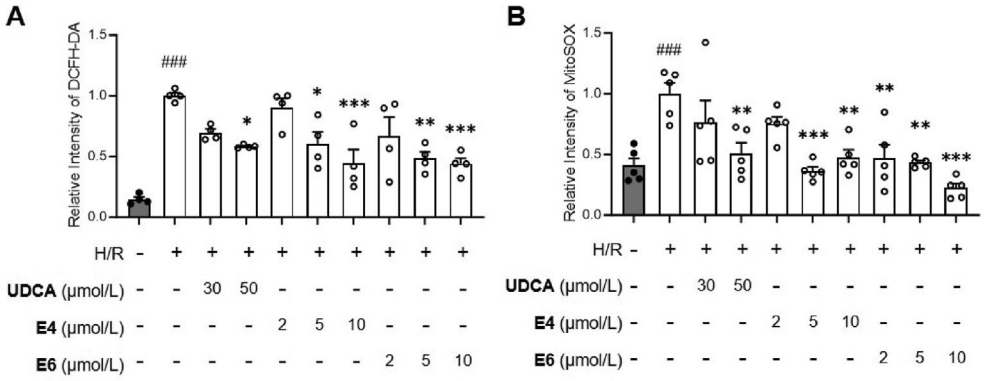

Figure 7 ROS scavenging activity of indicated compounds in NMCMs exposed to H/R. (A) intracellular ROS ($n = 4$) and (B) mitochondrial ROS ($n = 5$) levels were evaluated using DCFH-DA (2',7'-dichlorodihydrofluorescein diacetate) staining and MitoSOX Red mitochondrial superoxide indicator, respectively. Results are presented as mean ± SEM. $^{###}P < 0.001$ *vs.* normoxia vehicle control; $^{*}P < 0.05$, $^{**}P < 0.01$, $^{***}P < 0.001$ *vs.* H/R vehicle control.

phosphorylated PKA substrates—key downstream effectors of TGR5 (Supporting Information Fig. S11A and S11B), and concurrently suppressed FXR-SHP expression (Fig. S11C). These dual regulatory actions conferred superior cytoprotective effects in H/R-injured NMCMs compared to the respective mono-target modulators (Fig. S11D and S11E). Encouragingly, this therapeutic superiority was successfully replicated in a murine I/R model, where oral administration of **E6** (10 mg/kg) resulted in greater enhancement of systolic function, as evidenced by improved LVEF and LVFS, relative to mono-regulators INT-777 and GS (Fig. S11F−S11H).

To explore the therapeutic mechanisms underlying **E6** activity, bulk RNA sequencing (RNA-seq) was performed to assess cardiac transcriptional changes following treatment. Left ventricular (LV) tissues from mice pretreated with oral **E6** (10 mg/kg) or vehicle were collected after 24-h reperfusion. RNA-seq data underwent rigorous quality control, principal component analysis (PCA) and differential expression gene (DEG) analysis. Results revealed that **E6** treatment significantly altered LV transcriptomic profiles (Fig. 11A−B). Functional enrichment analysis showed these DEGs were primarily enriched in nutrient metabolism pathways[33,65] (Fig. 11C−D, Supporting Information Fig. S12). Further validation experiments were conducted in H/R-injured NMCMs using shTGR5 or AdFXR as genetic interventions (Supporting Information Figs. S13−S15). Given the established role of *Il10* in MIRI[66], we specifically examined its expression and found that **E6**-induced upregulation of *Il10* involved contributions from both

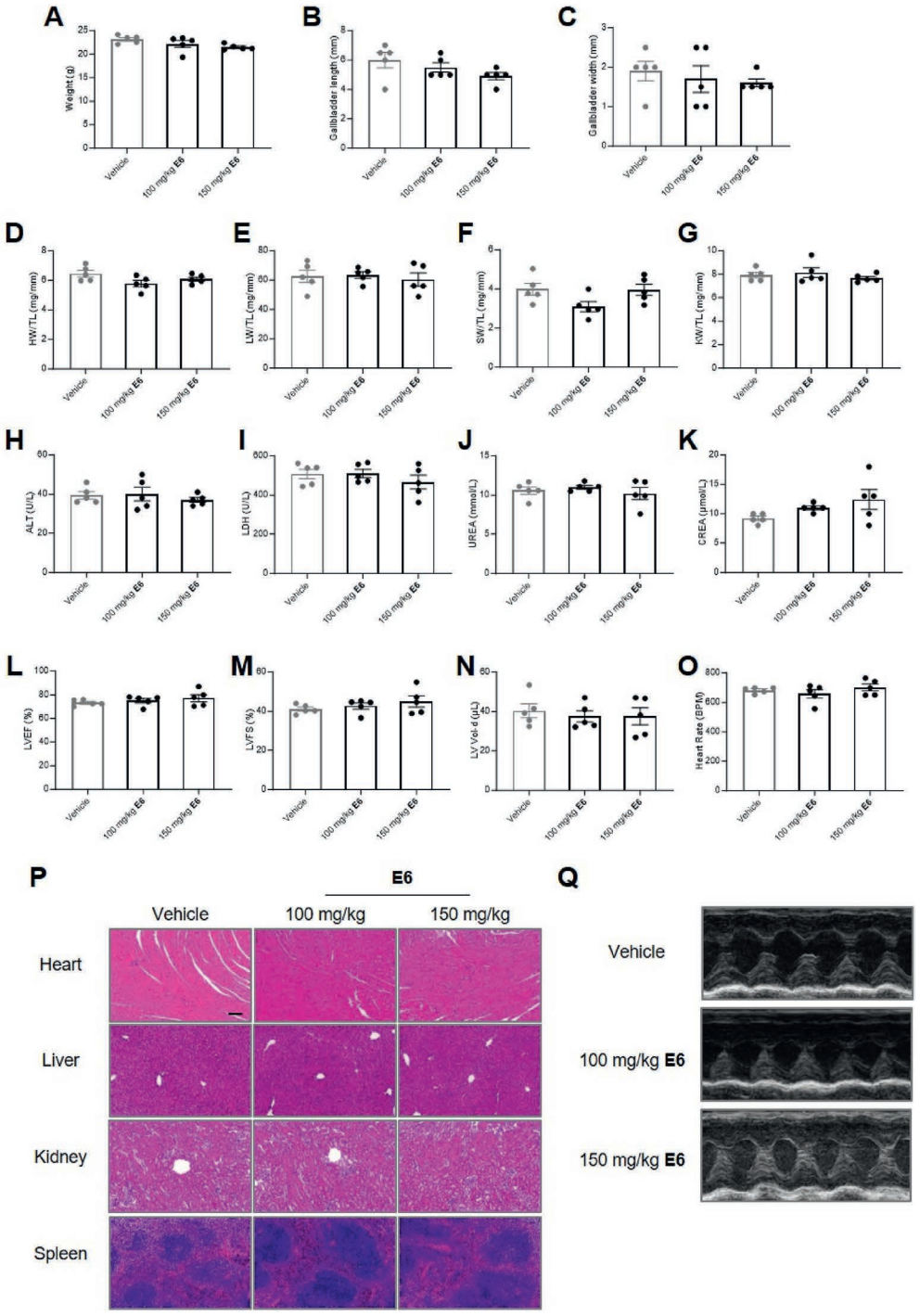

Figure 8 Subacute toxicity evaluation of compound **E6** *in vivo*. Mice received daily oral administration of vehicle or **E6** (100 or 150 mg/kg/day) for 7 consecutive days. Assessed parameters included: (A) body weight, (B, C) gallbladder dimensions, (D) heart weight, (E) liver weight, (F) spleen weight, (G) kidney weight, and (H−K) serum biochemical profiles. (L−O, Q) Echocardiographic assessments and (P) H&E-stained histopathological sections of major organs were analyzed. Scale bar = 100 μm. Data represent mean ± SEM (n = 5).

TGR5 and FXR signaling (Supporting Information Fig. S14A). Additionally, the regulation of *Rps6ka5*, and *Pdk1* by **E6** was primarily mediated through FXR (Fig. S14B and S14C). Collectively, these findings demonstrate that **E6** protects cardiomyocyte viability through coordinated modulation of both TGR5 and FXR, while also regulating apoptosis, inflammation, and lipid metabolism pathways.

The effects of **E6** on fatty acid uptake and lipid accumulation were further measured in NMCMs and cardiac sections. As shown in Supporting Information Fig. S16, fatty acid uptake was significantly reduced under H/R conditions (Fig. S16A and S16B), whereas neither intracellular lipid accumulation (Fig. S16C and S16D) nor cardiac lipid deposition in the *in vivo* MIRI model showed significant change (Fig. S16E and S16F). Treatment with

Table 6 Pharmacokinetic parameters of compound **E6** in ICR mice.

Compd.	Admi.	C_{max} (ng/mL)	$AUC_{0-\infty}$ (h·ng/mL)	$MRT_{0-\infty}$ (h)	T_{max} (h)	$t_{1/2}$ (h)	V_{ss} (L/kg)	CL (L/h/kg)	F (%)
E6[a]	i.v.	356.69	144.23	0.46	0.08	1.03	3.17	6.96	–
	p.o.	355.29	556.53	1.47	0.33	1.20	–	–	38.58

[a]Dosing regimens: intravenous (i.v.) 1 mg/kg and oral (*p.o.*) 10 mg/kg ($n = 3$ per group).

E6 partially restored fatty acid uptake without altering overall lipid accumulation, suggesting that **E6** primary modulates energy metabolism in cardiomyocytes rather than promoting lipid storage.

3. Discussions and conclusions

Myocardial ischemia/reperfusion injury remains a significant clinical challenge, with metabolic dysregulation limiting the efficacy of existing treatments. MIRI affects multiple cardiac pathways, including inflammation, oxidative stress, and substrate utilization. Therefore, effective pharmacological interventions should focus on optimizing cardioprotection while enhancing the efficacy of reperfusion. A bifunctional modulator that simultaneously activates TGR5 and antagonizes FXR presents a promising therapeutic strategy by integrating cardioprotection with metabolic regulation. In this study, structurally optimized **T26** derivatives were developed to achieve dual TGR5/FXR modulation, with sulfonyl benzoic acid incorporation emerging as a key feature for enhancing FXR antagonism *via* hydrogen bonding. Among them, the representative compound **E6** exhibited potent protection against H/R injury *in vitro*, markedly improving cardiomyocyte viability and reducing ROS accumulation. In MIRI mice, **E6** treatment significantly reduced infarct size and improved systolic function. Notably, **E6** outperformed mono-regulators in restoring LV function, potentially through its effects on modulation of inflammatory response, reduction of ROS production and attenuation of cellular apoptosis.

Dual modulation of TGR5 and FXR by **E6** offers synergistic benefits over single-target approaches by simultaneously addressing multiple pathological pathways in MIRI. FXR has been implicated in promoting apoptosis and metabolic dysregulation in ischemic tissues. Previous studies indicate that FXR activation mediates cardiomyocyte apoptosis[33,67], and its knockout confers protection against ischemic injury[68]. Consistently, our qPCR validation showed that **E6** downregulated *Rps6ka5 via* FXR antagonism. Inhibition of ribosomal S6 kinase is known to attenuate MIRI[69], suggesting that **E6** enhances cardiomyocyte survival partly through this mechanism. In addition, **E6** modulated *Pdk1* expression through FXR, a gene associated with inflammation[70], fatty acid utilization[71], and cardiac remodeling[72].

TGR5 primarily regulates inflammation in MIRI. Previous studies demonstrated that TGR5 activation mitigates inflammation and improves cardiac function[23,24]. Our data further show that **E6** upregulates *Il10*, a key anti-inflammatory cytokine, through modulation of both TGR5 and FXR, highlighting immune regulation as a critical point of synergy. *Il10* upregulation is a well-established downstream effect of TGR5 activation, consistent with its documented cardioprotective role in MIRI[24] and in NAFLD-related cardiovascular contexts[73]. In the FXR pathway, prior studies indicate that FXR deficiency elevates hepatic IL-10 under certain inflammatory conditions[74], while the FXR agonist obeticholic acid suppresses *Il10* expression during the middle phase of acute liver injury[75], suggesting that FXR antagonism by **E6** may contribute to *Il10* induction in a context-dependent manner. Collectively, these findings demonstrate that **E6** exerts cardioprotective effects by concurrently improving metabolism, reducing apoptosis, and fine-tuning inflammatory responses, underscoring the translational potential of dual TGR5/FXR modulation.

Beyond mechanistic insights, **E6** also demonstrates promising efficacy and a favorable safety profile. In the MIRI model, **E6** significantly improved left ventricular systolic function, as indicated by increased LVEF and LVFS, suggesting potential clinical benefits for patients with pre-existing cardiac impairment[76]. At the molecular level, **E6** reduced H/R-induced ROS production, suggesting protection against mitochondrial dysfunction, a key contributor to ischemia–reperfusion injury in diabetic hearts[77]. Importantly, **E6** did not induce gallbladder-related adverse effects commonly observed with classical TGR5 agonists, and its non-steroidal scaffold may avoid pruritus associated with bile acid metabolites[78]. Furthermore, as a single dual-targeting agent, **E6** offers advantages over multi-drug regimens by simplifying clinical administration, improving patient compliance, reducing the risk of drug–drug interactions, and providing more predictable pharmacokinetic and pharmacodynamic profiles[16].

Although **E6** directly engages both TGR5 (Supporting Information Fig. S17) and FXR (Fig. S3G), its activity still requires further optimization. Mechanistically, the protective effect of **E6** was dependent on both targets, as simultaneous *Tgr5* knockdown and *Fxr* overexpression significantly attenuated **E6**-mediated protection ($P = 0.0177$, Supporting Information Fig. S18), confirming that both TGR5 activation and FXR inhibition jointly contribute to its cardioprotective effects. Nevertheless, the observation that **E6** retains activity suggests that additional mechanisms beyond direct modulation of these two targets may also be involved.

Collectively, these results underscore the therapeutic potential of concurrent TGR5 activation and FXR inhibition. Our work identifies **E6** as a promising bifunctional lead compound for MIRI treatment and provides mechanistic insights into its cardioprotective effects.

4. Experimental

4.1. *In silico experiments*

4.1.1. *Virtual screening and molecular docking*

4.1.1.1. Protein and ligand preparation. All ligand–protein molecular docking simulations were performed using Schrödinger 2018. Protein structures were prepared with the *Protein Preparation Wizard* using default settings. The docking site was determined using *Receptor Grid Generation* in Glide, where the orthosteric ligands (P395 or INT-777 in TGR5, or NDB in FXR)

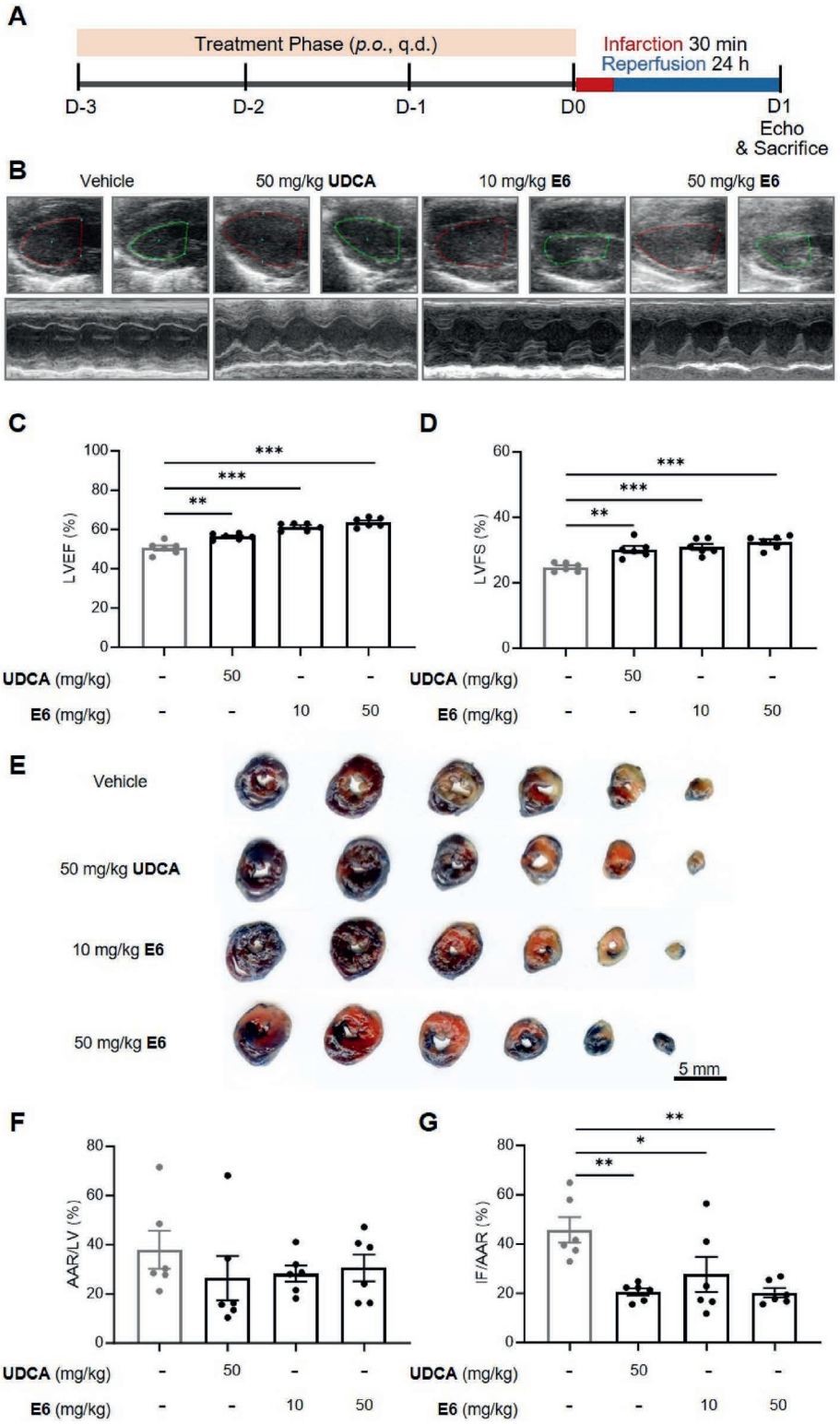

Figure 9 Protective effects of compound **E6** pretreatment against myocardial ischemia/reperfusion (I/R) injury in mice. Animals received oral administration of **E6** (10 or 50 mg/kg/day) for three consecutive days prior to I/R surgery. (A) Schematic of compound administration and surgical procedures. (B) Representative echocardiographic images, (C) left ventricular ejection fraction (LVEF) and (D) left ventricular fraction shortening (LVFS) measured at 24 h post-I/R. (E) Representative TTC/Evans Blue-stained sections and (F, G) infarct size quantification. Scale bar = 5 mm. Data represent mean ± SEM ($n = 6$). *$P < 0.05$, **$P < 0.01$, ***$P < 0.001$ *vs.* vehicle-treated I/R group.

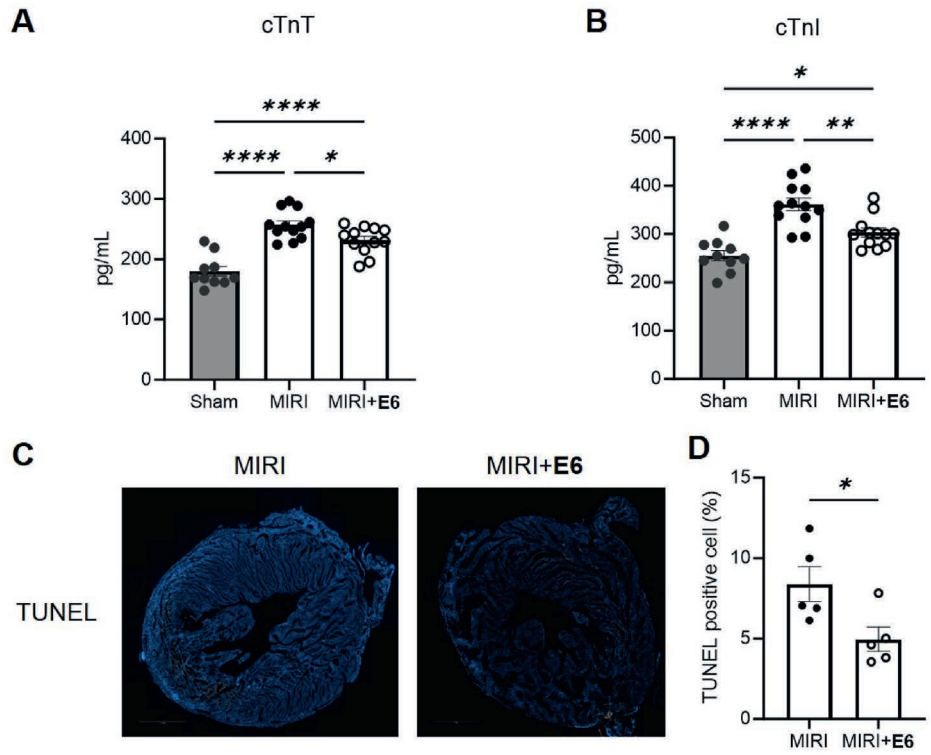

Figure 10 Clinical potential of E6 in MIRI mice model. Serum levels of cTnT (A), cTnI (B) were measured by ELISA. Results are presented as mean ± SEM ($n = 10$ for sham group, $n = 12$ for MIRI and E6 groups). *$P < 0.05$, **$P < 0.01$, ****$P < 0.0001$. (C) Representative TUNEL-stained heart sections acquired by high-content imaging. (D) Quantification of TUNEL-positive nuclei as a percentage of total nuclei. Results are presented as mean ± SEM ($n = 5$). *$P < 0.05$.

were selected as centroids and size references. Ligands were prepared with *LigPrep*, generating possible states at pH 7.0 ± 2.0; other parameters remained at default.

4.1.1.2. TGR5-based virtual screening. For TGR5 model selection, the chemical structures of P395 and INT-777 were drawn in ChemDraw and imported into Schrödinger for ligand preparation. These ligands were redocked into their corresponding cryo-EM structures. Redocking performance was evaluated based on: (1) the RMSD between the docked and original cryo-EM ligand conformations, and (2) the ability to reproduce key interactions. Virtual screening was conducted using Glide *Ligand Docking* (XP mode), with a maximum of 5 output poses per ligand. The poses were ranked and filtered by XP docking scores, followed by the application of *Pose Filter* to retain poses meeting both hydrogen-bond and aromatic interaction criteria. 2D similarity was calculated using MolPrint2D fingerprints in the *Canvas Similarity and Clustering* panel, and ligands were clustered into 150 groups based on Tanimoto coefficients.

4.1.1.3. T26 binding mode prediction. For inactive FXR structure selection, the poses of ivermectin (PDB: 4WVD) and NDB (PDB: 4OIV) were extracted from co-crystal structures. Pharmacophore similarity between **T26** and these reference ligands was assessed through pharmacophore type volume scoring in *Shape Screening*. Induced-fit docking of **T26** was performed to predict TGR5/FXR binding modes. In the *Induced Fit Docking* panel, the box center was defined by the **T26** centroid with a 20 Å box size, and all other parameters were kept at default.

4.1.2. Molecular dynamic simulations

4.1.2.1. System setup and preparation. Molecular dynamics (MD) simulations were conducted using the Desmond Molecular Dynamics module in Schrödinger 2018. Induced-fit docking of **E6** into both TGR5 and FXR was performed, and representative complexes were selected as the input for MD simulations. The system was prepared using the *System Builder* with the Optimized Potentials for Liquid Simulations-3 (OPLS3) force field to describe atomic interactions, while water molecules were modeled using the explicit Transferable Intermolecular Potential with 3 Points (TIP3P) solvent model. For TGR5 structures, a lipid bilayer environment was constructed using palmitoyl-oleoyl-phosphatidylcholine (POPC), with transmembrane residues identified from GPCRdb (https://gpcrdb.org/). An orthorhombic box was selected and subsequently minimized. The systems were neutralized by adding counterions and maintained in an isotonic 0.15 mol/L NaCl environment.

4.1.2.2. MD simulations. 50-ns MD simulations were performed using the *Molecular Dynamics* module with a recording interval of 5 ps. All simulations were performed under an *NPT* ensemble at 300 K and 1.01325 bar. Trajectory analysis was performed using the *Simulation Interaction Diagram* panel, yielding reports on protein/ligand RMSD and protein−ligand contact analyses. Representative binding modes were extracted

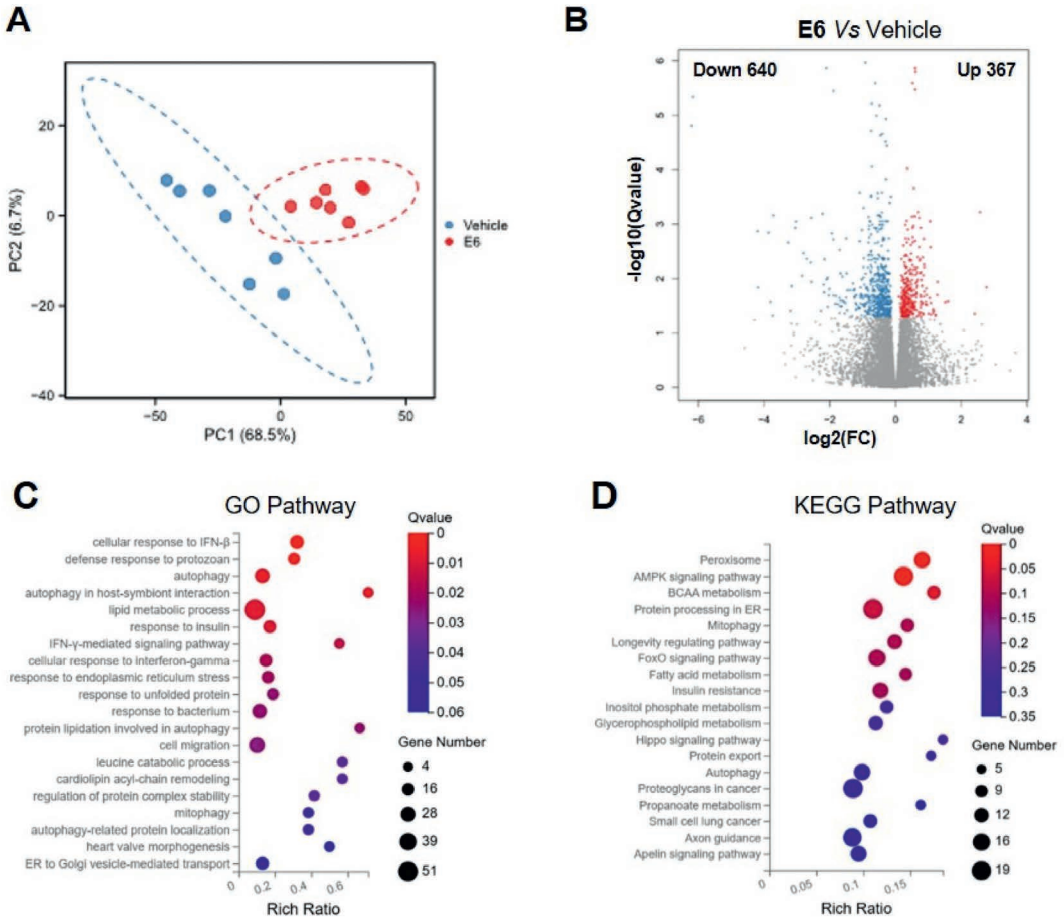

Figure 11 Transcriptomic profiling of ischemic myocardium in response to compound **E6** treatment. (A) Principal component analysis (PCA) demonstrating segregation between vehicle- and **E6**-treated groups. (B) Volcano plot of differentially expressed genes (DEGs). (C) Top enriched Gene Ontology (GO) pathways among DEGs. (D) Top enriched KEGG pathways among DEGs.

from the stable simulation phase. All structural visualizations were prepared using PyMOL (version 2.1.0).

4.2. *Chemistry*

All commercially available solvents and reagents were used without further purification. Reaction mixtures were purified by flash chromatography on silica gel (200−300 mesh), with products detected by UV (254 nm) or by alkaline potassium permanganate ($KMnO_4$) staining followed by heating. Nuclear magnetic resonance (^1H and ^{13}C NMR) spectra were recorded on Bruker AVANCE III-400 [^1H NMR (400 MHz), ^{13}C NMR (101 MHz)] or Bruker AVANCE NEO 600 [^1H NMR (600 MHz), ^{13}C NMR (150 MHz)] spectrometers. Chemical shifts (δ) are reported in parts per million (ppm) and referenced to residual solvent peaks: DMSO-d_6 (^1H: 2.50, ^{13}C: 39.52), $CDCl_3$ (^1H: 7.26, ^{13}C: 77.16). Spectral data were processed with MestreNova software (version 14.0.0), with peak multiplicities designated as: s (singlet), d (doublet), t (triplet), q (quartet), dt (doublet of triplets), td (triplets of doublets), m (multiplet), and brs (broad singlet). Coupling constant (J) values are reported in Hertz (Hz).

HPLC analysis was performed on an Agilent 1260 HPLC System (Angilent Technologies) equipped with an EC-C18 column (4.6 mm × 150 mm, 4 μm) at 1.2 mL/min and 30 °C (injection volume: 5 μL). Purity was determined by UV detection at 254 nm using the following mobile phases: (A) H_2O, (B) 5 mmol/L ammonium acetate in H_2O, and (D) acetonitrile. Two methods were employed: Method A used a gradient of 10%−90% D in A over 10 min; Method B used a gradient of 10%−90% D in B over 10 min. All tested compounds showed ≥95% purity.

High resolution mass spectra (HRMS) were acquired on a Waters XEVO G2 QTOF mass spectrometer at Peking University Medical and Health Analysis Center, reporting exact masses for $[M+H]^+$ or $[M-H]^-$ ions. Melting points were determined using a Büchi M-560 apparatus.

Additional synthetic procedures and the preparation of **T26** derivatives are provided in the Supporting Information

4.3. *Biology*

4.3.1. *Surface plasmon resonance (SPR) assay*

Binding of compounds to hFXRα-LBD were analyzed using Biacore T200 system (GE Healthcare, Chicago, IL, USA). Purified hFXRα-LBD protein was immobilized on a carboxymethylated 5 sensor chip using a standard amine coupling method. Different concentrations of E4, E5, E6 in running buffer were injected as analytes. Interaction parameters of K_D were determined using the Biacore Evaluation Software (T200 Version 2.0) based on the steady-state affinity model.

4.3.2. Cell culture and treatment

4.3.2.1. Cells and culture. NMCMs were isolated from 1-day-old C57BL/6 mice using established protocols[21]. HEK293, HEK293T, H9c2, and AC16 cells, along with NMCMs, were maintained in DMEM supplemented with 10% fetal bovine serum (FBS), 100 U/mL penicillin, and 100 μg/mL streptomycin under standard culture conditions (37 °C, 5% CO_2).

4.3.2.2. Hypoxia and reoxygenation procedures. Cells were incubated in high-glucose DMEM (4.5 mg/mL) at 37 °C in a standard incubator (95% air, 5% CO_2) for normoxia/reoxygenation conditions. For hypoxic conditions, cells were cultured in low-glucose DMEM (1 mg/mL) in a hypoxia chamber (95% N_2, 5% CO_2; $O_2 < 1\%$). For hypoxia/reoxygenation (H/R) experiments, cells were subjected to hypoxia (H) for 18 h followed by reoxygenation (R) for 6 h, with test compounds administered continuously throughout the 24-h H/R period.

4.3.3. GloSensor™ cAMP assay

The GloSensor cAMP assay was performed as previously described[47]. HEK293 cells transfected with FLAG-tagged human TGR5 and the GloSensor plasmid were seeded into 96-well culture plates and incubated for 48 h. Cells were stimulated with serum-free medium, which contained the GloSensor™ cAMP regent (Promega). Subsequently, the cells were stimulated with increasing concentrations of ligands for at least 5 min at room temperature. Luminescence per well was measured using a multimode plate reader (PerkinElmer EnVision). Data were analysed using the sigmoidal dose-response curve fitting in GraphPad Prism 7.0.

4.3.4. FXR TR-FRET assay

TR-FRET was measured using the LanthaScreen™ TR-FRET FXR Coactivator Assay (Invitrogen). All reagents were prepared according to the manufacturer's guidelines, and the compound incubation time was set to 10 h at 384-well plate. In the agonist assay, the relative agonistic activity was calculated as Eq. (1):

$$\text{Relative agonistic activity (\%)} = [(\text{Compound} - \text{DMSO})/(\text{CDCA} - \text{DMSO})] \times 100 \quad (1)$$

In the antagonistic assay, a final concentration of 50 μmol/L CDCA was mixed with the test compounds to determine FXR antagonistic efficacy, and the relative antagonistic rate was calculated as Eq. (2):

$$\text{Relative antagonistic rate (\%)} = \{1 - (\text{Compound} - \text{DMSO})/(\text{CDCA} - \text{DMSO})]\} \times 100 \quad (2)$$

4.3.5. Cell viability assay

The Cell Counting Kit-8 (CCK-8) assay (LABLEAD, CK001) was used to evaluate the cytotoxity and cardioprotective effects of the compounds. Cells were cultured in 96-well plates for 24 h before treatment with the indicated compounds under specific conditions. Subsequently, 10% (*v*/*v*) CCK-8 reagent was added to each well (final volume: 100 μL per well), and the plates were incubated for 2 h at 37 °C with 5% CO_2. Absorbance was measured at 450 nm, and cell viability was calculated as Eq. (3):

$$\text{Cell viability (\%)} = [(\text{Compound group})/(\text{DMSO control group})] \times 100 \quad (3)$$

In H/R experiments, cell viability was calculated as Eq. (4):

$$\text{Cell viability (\%)} = [(\text{Compound group under H/R conditions})/(\text{Compound group under normoxic conditions})] \times 100 \quad (4)$$

4.3.6. Dual luciferase reporter gene assay

HEK293T cells were cultured in 6-well plates until 70% confluency. The cells were co-transfected using Lipofectamine 2000 with pCMV plasmids encoding full-length human RXRα, FXRα, FXRE-luciferase, and Renilla. Subsequently, cells were cultured in DMEM supplemented with 10% FBS but without penicillin/streptomycin. After 20 h, cells were trypsinized and seeded into 96-well plates for 20-h compound treatment in Opti-MEM. A final concentration of 10 μmol/L CDCA was mixed with the test compounds to determine FXR antagonistic efficacy. After treatment, cells were lysed using Dual-Luciferase® Reporter Assay System (Promega), and luminescence per well was read on a microplate reader (SpectraMax iD5). Relative luciferase activity was calculated as (compound group)/(DMSO control group).

4.3.7. ROS detection

Intracellular and mitochondrial ROS production were assessed using the DCFH-DA probe (Beyotime, S0033S) and MitoSOX Red Mitochondrial Superoxide Indicator (MCE, HY-D1055), respectively. After treatment with the indicated compounds and exposure to H/R, NMCMs were incubated with 10 μmol/L DCFH-DA or MitoSOX Red at 37 °C for 15 min. After washing three times with PBS, nuclei were stained using Hoechst. Fluorescence was detected at 488/525 nm for intracellular ROS and 510/580 nm for mitochondrial ROS.

4.3.8. Western blot assay

Protein samples were extracted from NMCMs with RIPA lysis buffer (Solarbio, R0010) containing protease/phosphatase inhibitors. The proteins were separated using 10% SDS-PAGE and transferred onto a nitrocellulose membrane. The membranes were then blocked with 5% skim milk for 1 h and incubated overnight with primary antibodies against phospho-PKA substrate (Cell Signaling Technology, 9621S), SHP (Immunoway, YN0999) and GAPDH (Cell Signaling Technology, 5174S). After incubation with primary antibodies, the membranes were incubated with the corresponding secondary antibodies and visualized using ECL detection reagents (Millipore, WBKLS0500).

4.3.9. Animal study

All procedures related to animals were approved by the Peking University Biomedical Ethics Committee (LA2021591), and conducted in accordance with the Guide for the Care and Use of Laboratory Animals. Male C57BL/6 mice, aged 8−12 weeks and weighed 20−25 g, were purchased from Beijing Vital River Laboratory Animal Technology Co., Ltd. All mice were housed with ad libitum access to food and water and maintained in a specific pathogen-free animal facility at an ambient temperature of 22 °C and 50% humidity under a 12/12-h light-dark cycle.

4.3.9.1. Oral subacute toxicity assay. Compound dosages were freshly prepared in a mixed formula consisting of 18% isopropyl myristate, 33.5% polyoxyethylene (35) castor oil, 33.5% Labrasol® and 15% diethylene glycol monoethyl ether. Mice were

orally dosed for 7 days before echocardiography with a 30 MHz transducer (Vevo 2100 system, Fujifilm VisualSonics) and then sacrificed. The serum samples were collected and analyzed using a Toshiba TBA-120FR Automated Clinical Chemistry Analyzer. The heart, liver, spleen and kidney were harvested and fixed in 4% paraformaldehyde (PFA) overnight. After dehydration and embedding in paraffin, the tissues were sectioned into 5-μm-thick sections and stained with hematoxylin and eosin (H&E).

4.3.9.2. Single dose PK study. A single-dose pharmacokinetic (PK) study was conducted by Medicilon Preclinical Research (Shanghai) LLC. Briefly, male ICR mice received compound **E6** at 1 mg/kg (intravenous, i.v.) or 10 mg/kg (oral, *p.o.*, after fasting). Blood samples (approximately 30 μL) were collected at 0.083, 0.25, 0.5, 1, 2, 4, 8, and 24 h (i.v.), or 0.25, 0.5, 1, 2, 4, 6, 8, and 24 h (*p.o.*) after administration ($n = 3$ mice per time point). The samples were collected in sodium heparin tubes and centrifuged at $6800\times g$ for 6 min at 4 °C to obtain plasma. Plasma concentrations of **E6** were quantified using high-performance liquid chromatography tandem mass spectrometry (HPLC−MS/MS). Non-compartmental pharmacokinetic parameters were derived using WinNonlin® Professional 5.2 software.

4.3.9.3. MIRI mice experiments. Male C57BL/6 mice were orally dosed with compounds for three consecutive days prior to MIRI surgery. During MIRI surgery, the left anterior descending coronary artery was occluded approximately 2 mm away from its origin for 30 min and then loosened for 24 h and the ligation of the coronary artery was verified by electrocardiography with ST elevation. To assess myocardial infarct size, the hearts were first perfused with 0.5% Evans blue dye (Macklin, C10154250) to delineate the area at risk (AAR, unstained region), then frozen at −20 °C for 30 min and sectioned into six 1-mm-thick slices. The slices were subsequently incubated in 2% TTC reagent (Solarbio, G3005) for 30 min to visualize the infarct size (IF). The infarct and left ventricular (LV) areas were determined by automatic planimetry with Image-Pro Plus software (version 6.0, Media Cybernetics, Inc).

4.3.10. RNA sequencing

Total RNA was extracted from heart tissue after myocardial I/R injury using TRIzol reagent. The RNA was then reverse-transcribed into cDNA to construct a strand-specific mRNA library. The sequencing data were cleaned by removing reads that contained sequencing adapters, had >20% low-quality bases, or contained >5% unknown bases. The subsequent analysis was performed using the Dr. Tom Multi-omics Data mining system (https://biosys.bgi.com). The differentially expressed genes (DEGs) were identified using DESeq2 with a threshold of adjusted $P < 0.05$. GO and KEGG enrichment analyses were performed using Phyper (hypergeometric test).

4.3.11. Statistical analysis

The experimental data were analyzed using GraphPad Prism 9 (version 9.4.1, GraphPad Software Inc.) and were presented as mean ± standard error of the mean (SEM). The Shapiro-Wilk test was used to evaluate the normal distribution of data. The two-tailed Student's *t*-test and Mann-Whitney test were employed to analyze differences between two groups with normally distributed and non-normally distributed data, respectively. One-way ANOVA followed by Tukey's post hoc multiple comparison test was used for comparisons among multiple groups. Statistical significance was set at $P < 0.05$.

Acknowledgments

We acknowledge financial support from the National Natural Science Foundation of China (Nos. 22131002, 22161142019, 22293014, 22207009, T2450076, and 82270343), the National Key R&D Program of China (No. 2021YFA1501700), Fundamental and Interdisciplinary Disciplines Breakthrough Plan of the Ministry of Education of China (JYB2025XDXM603), the Peking University Medicine plus X Pilot Program-Key Technologies R&D Project (No. 2024YXXLHGG001, China), the New Cornerstone Science Foundation, the XPLORER PRIZE, the Natural Science Foundation of Beijing (Nos. L248019 and 7252197, China), the CAMS Innovation Fund for Medical Sciences (No. 2021-I2M-5-003, China), and the support from "Laboratory for Synthetic Chemistry and Chemical Biology" under the Health@InnoHK Program. We would like to express our gratitude to the staff of Center of Basic Medical Research, Institute of Medical Innovation and Research, Peking University Third Hospital for their assistance during the process of conducting this project.

Author contributions

Ning Jiao and Ming Xu conceived and directed the project. Xinyi Zhao and Tianqi Chang wrote the manuscript, which was revised by Ning Jiao, Ming Xu, Xiaodong Dou, Jin-Peng Sun and Jiaxing Wang. Xinyi Zhao performed the *in-silico* experiments, compound design and synthesis, and FXR evaluation; Xiang Wu conducted the TGR5 evaluation; Tianqi Chang and Xinyi Zhao conducted the *in vitro* pharmacological experiments; Tianqi Chang, Jiaxing Wang and Tongyu Huo conducted the animal experiments; Tongyu Huo contributed to compound design and synthesis; Jing Peng contributed to compound synthesis, purification, HPLC analysis and melting point testing; Dongfang Li and Fan Yang contributed to the TGR5 FlAsH-BRET assay; Xiaodong Dou, Yameng Liu and Chao Wang provided experimental technical supports. All authors critically reviewed and approved the final manuscript.

Conflicts of interest

The authors declare no conflicts of interest.

Appendix A. Supporting information

Supporting information to this article can be found online at https://doi.org/10.1016/j.apsb.2026.03.038.

References

1. Word Health Organization. *The top 10 causes of death*. Available from: https://www.who.int/news-room/fact-sheets/detail/the-top-10-causes-of-death.
2. Tsao CW, Aday AW, Almarzooq ZI, Anderson CAM, Arora P, Avery CL, et al. Heart disease and stroke statistics—2023 update: a

report from the American heart association. *Circulation* 2023;**147**: e93−621.
3. Szummer K, Wallentin L, Lindhagen L, Alfredsson J, Erlinge D, Held C, et al. Improved outcomes in patients with ST-elevation myocardial infarction during the last 20 years are related to implementation of evidence-based treatments: experiences from the SWEDEHEART registry 1995−2014. *Eur Heart J* 2017;**38**:3056−65.
4. Heusch G. Myocardial ischaemia−reperfusion injury and cardioprotection in perspective. *Nat Rev Cardiol* 2020;**17**:773−89.
5. Liu TL, Hao Y, Zhang ZX, Zhou H, Peng SQ, Zhang DY, et al. Advanced cardiac patches for the treatment of myocardial infarction. *Circulation* 2024;**149**:2002−20.
6. Xiang Q, Yi X, Zhu XH, Wei X, Jiang DS. Regulated cell death in myocardial ischemia−reperfusion injury. *Trends Endocrinol Metabol* 2024;**35**:219−34.
7. van Royen N, Escaned J, Riksen NP, Berry C, van Geuns R-JM, Nijveldt R, et al. Pathophysiology and diagnosis of coronary microvascular dysfunction in ST-elevation myocardial infarction. *Cardiovasc Res* 2020;**116**:787−805.
8. Beijnink CWH, van der Hoeven NW, Konijnenberg LSF, Kim RJ, Bekkers SCAM, Kloner RA, et al. Cardiac MRI to visualize myocardial damage after ST-segment elevation myocardial infarction: a review of its histologic validation. *Radiology* 2021;**301**:4−18.
9. Heusch G. Myocardial ischemia/reperfusion: translational pathophysiology of ischemic heart disease. *Med* 2024;**5**:10−31.
10. Welt FGP, Batchelor W, Spears JR, Penna C, Pagliaro P, Ibanez B, et al. Reperfusion injury in patients with acute myocardial infarction. *J Am Coll Cardiol* 2024;**83**:2196. 13.
11. Mastoor Y, Murphy E, Roman B. Mechanisms of postischemic cardiac death and protection following myocardial injury. *J Clin Investig* 2025;**135**:e184134.
12. Davidson SM, Ferdinandy P, Andreadou I, Bøtker HE, Heusch G, Ibáñez B, et al. Multitarget strategies to reduce myocardial ischemia/reperfusion injury. *J Am Coll Cardiol* 2019;**73**:89−99.
13. Ferdinandy P, Hausenloy DJ, Heusch G, Baxter GF, Schulz R. Interaction of risk factors, comorbidities, and comedications with ischemia/reperfusion injury and cardioprotection by preconditioning, postconditioning, and remote conditioning. *Pharmacol Rev* 2014;**66**: 1142−74.
14. Johansson S, Rosengren A, Young K, Jennings E. Mortality and morbidity trends after the first year in survivors of acute myocardial infarction: a systematic review. *BMC Cardiovasc Disord* 2017;**17**: 53−60.
15. Yang TG, Zhang DQ. Research progress on the effects of novel hypoglycemic drugs in diabetes combined with myocardial ischemia/reperfusion injury. *Ageing Res Rev* 2023;**86**:101884.
16. Proschak E, Stark H, Merk D. Polypharmacology by design: a medicinal chemist's perspective on multitargeting compounds. *J Med Chem* 2018;**62**:420−44.
17. Fleishman JS, Kumar S. Bile acid metabolism and signaling in health and disease: molecular mechanisms and therapeutic targets. *Signal Transduct Targeted Ther* 2024;**9**:97−147.
18. Fan Y, Li Y, Chen Y, Zhao YJ, Liu LW, Li J, et al. Comprehensive metabolomic characterization of coronary artery diseases. *J Am Coll Cardiol* 2016;**68**:1281−93.
19. Li WY, Shu S, Cheng LL, Hao X, Wang LJ, Wu Y, et al. Fasting serum total bile acid level is associated with coronary artery disease, myocardial infarction and severity of coronary lesions. *Atherosclerosis* 2020;**292**:193−200.
20. Chong Nguyen C, Duboc D, Rainteau D, Sokol H, Humbert L, Seksik P, et al. Circulating bile acids concentration is predictive of coronary artery disease in human. *Sci Rep* 2021;**11**:22661−70.
21. Wang H, Wang JX, Cui H, Fan CY, Xue YZ, Liu HY, et al. Inhibition of fatty acid uptake by TGR5 prevents diabetic cardiomyopathy. *Nat Metab* 2024;**6**:1161−77.
22. Wang JX, Xu T, Xu M. Roles and mechanisms of TGR5 in the modulation of $CD4^+$ T cell functions in myocardial infarction. *J Cardiovasc Transl Res* 2021;**15**:350−9.
23. Wang JX, Zhang JS, Lin XJ, Wang YP, Wu X, Yang F, et al. DCA−TGR5 signaling activation alleviates inflammatory response and improves cardiac function in myocardial infarction. *J Mol Cell Cardiol* 2021;**151**:3−14.
24. Li JZ, Cheng RN, Wan H. Overexpression of TGR5 alleviates myocardial ischemia/reperfusion injury *via* AKT/GSK-3β mediated inflammation and mitochondrial pathway. *Biosci Rep* 2020;**40**. BSR20193482.
25. Qi ZY, Zhang W, Zhang P, Qu YN, Zhong HX, Zhou LN, et al. The gut microbiota−bile acid−TGR5 axis orchestrates platelet activation and atherothrombosis. *Nat Cardiovasc Res* 2025;**4**: 584−601.
26. Zhang QH, He FT, Kuruba R, Gao X, Wilson A, Li J, et al. FXR-mediated regulation of angiotensin type 2 receptor expression in vascular smooth muscle cells. *Cardiovasc Res* 2008;**77**:560−9.
27. Xia YL, Xu XY, Guo YZ, Lin C, Xu XM, Zhang FY, et al. Mesenchymal stromal cells overexpressing farnesoid X receptor exert cardioprotective effects against acute ischemic heart injury by binding endogenous bile acids. *Adv Sci (Weinh)* 2022;**9**:e2200431.
28. Li J, Wilson A, Kuruba R, Zhang QH, Gao X, He F, et al. FXR-mediated regulation of eNOS expression in vascular endothelial cells. *Cardiovasc Res* 2008;**77**:169−77.
29. Lu HL, Wu ZN, Wan M, Xiong SS, Huang X, Liu T, et al. Taurochenodeoxycholic acid alleviates obesity-induced endothelial dysfunction. *Eur Heart J* 2026;**47**:1221−38.
30. Mencarelli A, Cipriani S, Renga B, D'Amore C, Palladino G, Distrutti E, et al. FXR activation improves myocardial fatty acid metabolism in a rodent model of obesity-driven cardiotoxicity. *Nutr Metabol Cardiovasc Dis* 2013;**23**:94−101.
31. Wu Q, Sun LL, Hu XM, Wang XM, Xu F, Chen B, et al. Suppressing the intestinal farnesoid X receptor/sphingomyelin phosphodiesterase 3 axis decreases atherosclerosis. *J Clin Investig* 2021;**131**:e142865.
32. Gao JS, Liu XQ, Wang BJ, Xu HQ, Xia Q, Lu TF, et al. Farnesoid X receptor deletion improves cardiac function, structure and remodeling following myocardial infarction in mice. *Mol Med Rep* 2017;**16**: 673−9.
33. Pu J, Yuan AC, Shan PR, Gao EH, Wang XL, Wang YJ, et al. Cardiomyocyte-expressed farnesoid-X-receptor is a novel apoptosis mediator and contributes to myocardial ischaemia/reperfusion injury. *Eur Heart J* 2013;**34**:1834−45.
34. Pellicciari R, Gioiello A, Macchiarulo A, Thomas C, Rosatelli E, Natalini B, et al. Discovery of 6α-ethyl-23(*S*)-methylcholic acid (S-EMCA, INT-777) as a potent and selective agonist for the TGR5 receptor, a novel target for diabesity. *J Med Chem* 2009;**52**:7958−61.
35. Hodge RJ, Lin J, Vasist Johnson LS, Gould EP, Bowers GD, Nunez DJ. Safety, pharmacokinetics, and pharmacodynamic effects of a selective TGR5 agonist, SB-756050, in type 2 diabetes. *Clin Pharmacol Drug Dev* 2013;**2**:213−22.
36. Urizar NL, Liverman AB, Dodds DNT, Silva FV, Ordentlich P, Yan Y, et al. A natural product that lowers cholesterol as an antagonist ligand for FXR. *Science* 2002;**296**:1703−6.
37. Burris TP, Montrose C, Houck KA, Osborne HE, Bocchinfuso WP, Yaden BC, et al. The hypolipidemic natural product guggulsterone is a promiscuous steroid receptor ligand. *Mol Pharmacol* 2005;**67**: 948−54.
38. Dou XD, Huo TY, Liu YM, Pang ZC, Su LY, Zhao XY, et al. Discovery of novel and selective farnesoid X receptor antagonists through structure-based virtual screening, preliminary structure−activity relationship study, and biological evaluation. *Eur J Med Chem* 2024;**269**: 116323−36.
39. Rizzo G, Passeri D, De Franco F, Ciaccioli G, Donadio L, Rizzo G, et al. Functional characterization of the semisynthetic bile acid

derivative INT-767, a dual farnesoid X receptor and TGR5 agonist. *Mol Pharmacol* 2010;**78**:617−30.
40. Ding LL, Yang QL, Zhang EY, Wang YM, Sun SM, Yang YB, et al. Notoginsenoside Ft1 acts as a TGR5 agonist but FXR antagonist to alleviate high fat diet-induced obesity and insulin resistance in mice. *Acta Pharma Sin B* 2021;**11**:1541−54.
41. Lamers C, Merk D, Gabler M, Flesch D, Kaiser A, Schubert-Zsilavecz M. SAR studies on FXR modulators led to the discovery of the first combined FXR antagonistic/TGR5 agonistic compound. *Future Med Chem* 2016;**8**:133−48.
42. Makki K, Brolin H, Petersen N, Henricsson M, Christensen DP, Khan MT, et al. 6α-Hydroxylated bile acids mediate TGR5 signalling to improve glucose metabolism upon dietary fiber supplementation in mice. *Gut* 2023;**72**:314−24.
43. Stefela A, Kaspar M, Drastik M, Kronenberger T, Micuda S, Dracinsky M, et al. (*E*)-7-Ethylidene-lithocholic acid (7-ELCA) is a potent dual farnesoid X receptor (FXR) antagonist and GPBAR1 agonist inhibiting FXR-induced gene expression in hepatocytes and stimulating glucagon-like peptide-1 secretion from enteroendocrine cells. *Front Pharmacol* 2021;**12**:713149−67.
44. Tian FY, Chen TX, Xu WD, Fan YC, Feng XH, Huang Q, et al. Curcumin compensates GLP-1 deficiency *via* the microbiota-bile acids axis and modulation in functional crosstalk between TGR5 and FXR in *ob/ob* mice. *Mol Nutr Food Res* 2023;**67**:e2300195.
45. Zhai ZY, Niu KM, Liu HP, Lin C, Tu Y, Liu YC, et al. Policosanol alleviates hepatic lipid accumulation by regulating bile acids metabolism in C57BL6/mice through AMPK−FXR−TGR5 cross-talk. *J Food Sci* 2021;**86**:5466−78.
46. Zheng XJ, Chen TL, Jiang RQ, Zhao AH, Wu Q, Kuang JL, et al. Hyocholic acid species improve glucose homeostasis through a distinct TGR5 and FXR signaling mechanism. *Cell Metab* 2021;**33**:791−803.e7.
47. Yang F, Mao CY, Guo LL, Lin JY, Ming QQ, Xiao P, et al. Structural basis of GPBAR activation and bile acid recognition. *Nature* 2020;**587**:499−504.
48. Chen G, Wang XK, Ge YJ, Ma L, Chen Q, Liu HH, et al. Cryo-EM structure of activated bile acids receptor TGR5 in complex with stimulatory G protein. *Signal Transduct Targeted Ther* 2020;**5**:142−4.
49. Gertzen CGW, Spomer L, Smits SHJ, Häussinger D, Keitel V, Gohlke H. Mutational mapping of the transmembrane binding site of the G-protein coupled receptor TGR5 and binding mode prediction of TGR5 agonists. *Eur J Med Chem* 2015;**104**:57−72.
50. Macchiarulo A, Gioiello A, Thomas C, Pols TWH, Nuti R, Ferrari C, et al. Probing the binding site of bile acids in TGR5. *ACS Med Chem Lett* 2013;**4**:1158−62.
51. Jin LH, Feng XH, Rong H, Pan ZF, Inaba YK, Qiu L, et al. The antiparasitic drug ivermectin is a novel FXR ligand that regulates metabolism. *Nat Commun* 2013;**4**:1937−44.
52. Xu X, Xu X, Liu P, Zhu ZY, Chen J, Fu HA, et al. Structural basis for small molecule NDB (*N*-benzyl-*N*-(3-(*tert*-butyl)-4-hydroxyphenyl)-2,6-dichloro-4-(dimethylamino) Benzamide) as a selective antagonist of Farnesoid X Receptor α (FXRα) in stabilizing the homodimerization of the receptor. *J Biol Chem* 2015;**290**:19888−99.
53. Merk D, Sreeramulu S, Kudlinzki D, Saxena K, Linhard V, Gande SL, et al. Molecular tuning of farnesoid X receptor partial agonism. *Nat Commun* 2019;**10**:2915−28.
54. Jaladanki CK, Taxak N, Varikoti RA, Bharatam PV. Toxicity originating from thiophene containing drugs: exploring the mechanism using quantum chemical methods. *Chem Res Toxicol* 2015;**28**:2364−76.
55. Sato H, Macchiarulo A, Thomas C, Gioiello A, Une M, Hofmann AF, et al. Novel potent and selective bile acid derivatives as TGR5 agonists: biological screening, structure−activity relationships, and molecular modeling studies. *J Med Chem* 2008;**51**:1831−41.
56. Lew J-L, Zhao A, Yu JH, Huang L, de Pedro N, Peláez F, et al. The Farnesoid X Receptor controls gene expression in a ligand- and promoter-selective fashion. *J Biol Chem* 2004;**279**:8856−61.
57. Rajesh KG, Suzuki R, Maeda H, Yamamoto M, Yutong X, Sasaguri S. Hydrophilic bile salt ursodeoxycholic acid protects myocardium against reperfusion injury in a PI3K/Akt dependent pathway. *J Mol Cell Cardiol* 2005;**39**:766−76.
58. Zhang R, Ma WQ, Fu MJ, Li J, Hu CH, Chen Y, et al. Overview of bile acid signaling in the cardiovascular system. *World J Clin Cases* 2021;**9**:308−20.
59. Ale-Agha N, Jakobs P, Goy C, Zurek M, Rosen J, Dyballa-Rukes N, et al. Mitochondrial telomerase reverse transcriptase protects from myocardial ischemia/reperfusion injury by improving complex i composition and function. *Circulation* 2021;**144**:1876−90.
60. Hao T, Qian M, Zhang YT, Liu Q, Midgley AC, Liu YP, et al. An injectable dual-function hydrogel protects against myocardial ischemia/reperfusion injury by modulating ROS/NO disequilibrium. *Adv Sci (Weinh)* 2022;**9**:2105408−22.
61. Cao Q, Liu L, Hu YG, Cao S, Tan TT, Huang X, et al. Low-intensity pulsed ultrasound of different intensities differently affects myocardial ischemia/reperfusion injury by modulating cardiac oxidative stress and inflammatory reaction. *Front Immunol* 2023;**14**:1248056−72.
62. Jin WR, Zheng MY, Chen YH, Xiong H. Update on the development of TGR5 agonists for human diseases. *Eur J Med Chem* 2024;**271**:116462−81.
63. Choi M, Moschetta A, Bookout AL, Peng L, Umetani M, Holmstrom SR, et al. Identification of a hormonal basis for gallbladder filling. *Nat Med* 2006;**12**:1253−5.
64. Stedman C, Liddle C, Coulter S, Sonoda J, Alvarez JG, Evans RM, et al. Benefit of farnesoid X receptor inhibition in obstructive cholestasis. *Proc Natl Acad Sci U S A* 2006;**103**:11323−8.
65. Jiang CT, Xie C, Lv Y, Li J, Krausz KW, Shi JM, et al. Intestine-selective farnesoid X receptor inhibition improves obesity-related metabolic dysfunction. *Nat Commun* 2015;**6**:10166−83.
66. Yang Z, Zingarelli B, Szabó C. Crucial role of endogenous Interleukin-10 production in myocardial ischemia/reperfusion injury. *Circulation* 2000;**101**:1019−26.
67. Gao Y, Zhao YC, Yuan AC, Xu LW, Huang X, Su YY, et al. Effects of farnesoid-X-receptor SUMOylation mutation on myocardial ischemia/reperfusion injury in mice. *Exp Cell Res* 2018;**371**:301−10.
68. Shan HM, Zang MH, Zhang Q, Shi RB, Shi XJ, Mamtilahun M, et al. Farnesoid X receptor knockout protects brain against ischemic injury through reducing neuronal apoptosis in mice. *J Neuroinflammation* 2020;**17**:164.
69. Shi X, O'Neill MM, MacDonnell S, Brookes PS, Yan C, Berk BC. The RSK inhibitor BIX02565 limits cardiac ischemia/reperfusion injury. *J Cardiovasc Pharmacol Therapeut* 2015;**21**:177−86.
70. Forteza MJ, Berg M, Edsfeldt A, Sun J, Baumgartner R, Kareinen I, et al. Pyruvate dehydrogenase kinase regulates vascular inflammation in atherosclerosis and increases cardiovascular risk. *Cardiovasc Res* 2023;**119**:1524−36.
71. Atser MG, Wenyonu CD, Rowe EM, Leung CLK, Cen HH, Queathem ED, et al. Pyruvate dehydrogenase kinase 1 controls triacylglycerol hydrolysis in cardiomyocytes. *J Biol Chem* 2025;**301**:108398.
72. Amina S, Wei M, Zhang S, Jiaqi F, Ma S, Abbas MK, et al. Metabolism-related gene PDK1 regulates myocardial cell remodeling and its mechanism. *Stem Cell Res Ther* 2025;**16**:404.
73. Biagioli M, Marchianò S, Di Giorgio C, Bordoni M, Urbani G, Bellini R, et al. Activation of GPBAR1 attenuates vascular inflammation and atherosclerosis in a mouse model of NAFLD-related cardiovascular disease. *Biochem Pharmacol* 2023;**218**:115900.
74. Sotillo J, Zhang B, Li J, Zong X, Wang J, Xin L, et al. FXR deficiency in hepatocytes disrupts the bile acid homeostasis and inhibits autophagy to promote liver injury in *Schistosoma japonicum*-infected mice. *PLoS Neglected Trop Dis* 2022;**16**:e0010651.
75. Ding W, Fan YY, Zhang C, Fu L, Chen X, Xu DX. Obeticholic acid differentially regulates hepatic injury and inflammation at different

stages of D-galactosamine/lipopolysaccharide-evoked acute liver failure. *Eur J Pharmacol* 2019;**850**:150−7.
76. Zhang ZY, Fang XH, Liu CC, Wang CX, Liu HJ, Lu WB, et al. Ejection fraction indexed to left ventricular mass and its association with cardiac event risk in a community population with mildly reduced or preserved ejection fraction. *J Am Heart Assoc* 2025;**14**: e038777.
77. Rudokas MW, McKay M, Toksoy Z, Eisen JN, Bögner M, Young LH, et al. Mitochondrial network remodeling of the diabetic heart: implications to ischemia related cardiac dysfunction. *Cardiovasc Diabetol* 2024;**23**:261.
78. Yang J, Zhao TJ, Fan JP, Zou HB, Lan GY, Guo FS, et al. Structure-guided discovery of bile acid derivatives for treating liver diseases without causing itch. *Cell* 2024;**187**:7164-82.e18.